

Induction of myelodysplasia by myeloid-derived suppressor cells

Xianghong Chen, ... , Alan List, Sheng Wei

J Clin Invest. 2013;123(11):4595-4611. <https://doi.org/10.1172/JCI67580>.

Research Article

Hematology

Myelodysplastic syndromes (MDS) are age-dependent stem cell malignancies that share biological features of activated adaptive immune response and ineffective hematopoiesis. Here we report that myeloid-derived suppressor cells (MDSC), which are classically linked to immunosuppression, inflammation, and cancer, were markedly expanded in the bone marrow of MDS patients and played a pathogenetic role in the development of ineffective hematopoiesis. These clonally distinct MDSC overproduce hematopoietic suppressive cytokines and function as potent apoptotic effectors targeting autologous hematopoietic progenitors. Using multiple transfected cell models, we found that MDSC expansion is driven by the interaction of the proinflammatory molecule S100A9 with CD33. These 2 proteins formed a functional ligand/receptor pair that recruited components to CD33's immunoreceptor tyrosine-based inhibition motif (ITIM), inducing secretion of the suppressive cytokines IL-10 and TGF- β by immature myeloid cells. *S100A9* transgenic mice displayed bone marrow accumulation of MDSC accompanied by development of progressive multilineage cytopenias and cytological dysplasia. Importantly, early forced maturation of MDSC by either *all-trans-retinoic acid* treatment or active immunoreceptor tyrosine-based activation motif-bearing (ITAM-bearing) adapter protein (DAP12) interruption of CD33 signaling rescued the hematologic phenotype. These findings indicate that primary bone marrow expansion of MDSC driven by the S100A9/CD33 pathway perturbs hematopoiesis and contributes to the development of MDS.

Find the latest version:

<https://jci.me/67580/pdf>





Induction of myelodysplasia by myeloid-derived suppressor cells

Xianghong Chen,¹ Erika A. Eksioglu,¹ Junmin Zhou,¹ Ling Zhang,¹ Julie Djeu,¹ Nicole Fortenbery,¹ Pearlie Epling-Burnette,¹ Sandra Van Bijnen,² Harry Dolstra,² John Cannon,³ Je-in Youn,¹ Sarah S. Donatelli,¹ Dahui Qin,¹ Theo De Witte,² Jianguo Tao,¹ Huaquan Wang,⁴ Pingyan Cheng,¹ Dmitry I. Gabrilovich,¹ Alan List,¹ and Sheng Wei^{1,4}

¹H. Lee Moffitt Cancer Center, Tampa, Florida, USA. ²Radboud University Nijmegen Medical Centre, Nijmegen, The Netherlands. ³Department of Pediatrics, Children's Research Institute, University of South Florida, Tampa, Florida, USA. ⁴Tianjin Medical University Cancer Hospital, Tianjin, China.

Myelodysplastic syndromes (MDS) are age-dependent stem cell malignancies that share biological features of activated adaptive immune response and ineffective hematopoiesis. Here we report that myeloid-derived suppressor cells (MDSC), which are classically linked to immunosuppression, inflammation, and cancer, were markedly expanded in the bone marrow of MDS patients and played a pathogenetic role in the development of ineffective hematopoiesis. These clonally distinct MDSC overproduce hematopoietic suppressive cytokines and function as potent apoptotic effectors targeting autologous hematopoietic progenitors. Using multiple transfected cell models, we found that MDSC expansion is driven by the interaction of the proinflammatory molecule S100A9 with CD33. These 2 proteins formed a functional ligand/receptor pair that recruited components to CD33's immunoreceptor tyrosine-based inhibition motif (ITIM), inducing secretion of the suppressive cytokines IL-10 and TGF- β by immature myeloid cells. S100A9 transgenic mice displayed bone marrow accumulation of MDSC accompanied by development of progressive multilineage cytopenias and cytological dysplasia. Importantly, early forced maturation of MDSC by either *all-trans-retinoic acid* treatment or active immunoreceptor tyrosine-based activation motif-bearing (ITAM-bearing) adapter protein (DAP12) interruption of CD33 signaling rescued the hematologic phenotype. These findings indicate that primary bone marrow expansion of MDSC driven by the S100A9/CD33 pathway perturbs hematopoiesis and contributes to the development of MDS.

Introduction

Understanding the selective pressures and mechanisms involved in the initiation of stem cell malignancies is critical to development of effective strategies for prevention and treatment. Inflammatory molecules have long been implicated as regulatory cues driving the proliferation and apoptotic death of hematopoietic progenitors in myelodysplastic syndromes (MDS) (1–3). Chronic immune stimulation, coupled with senescence dependent changes in both hematopoietic stem/progenitor cells (HSPC) and the BM microenvironment, are believed to be critical to the pathogenesis of the disease (4). Increasing evidence implicates the activation of innate immune signaling in both hematopoietic senescence and the pathobiology of MDS (5). TLR4, for instance, is overexpressed in MDS BM HSPC and is implicated in progenitor apoptosis and subsequent development of cytopenias (6). Furthermore, gene expression of the TLR adaptor E3 ubiquitin ligase, TNF receptor-associated factor-6 (TRAF6), is markedly upregulated in MDS CD34⁺ cells (7) accompanied in some cases by amplification of genomic regions encoding TRAF6 or the Toll IL-1 receptor domain-containing adaptor protein (TIRAP), key intermediates in TLR4 signaling (8, 9). Recent investigations showed that TLR signaling is constitutively activated in MDS with chromosome 5q deletion [del(5q)] as a result of allelic deletion of microRNA 145 (miRNA-145) and

miRNA-146a and consequent upregulation of their respective targets, TIRAP and TRAF6 (10). Moreover, knockdown of these specific miRNAs or overexpression of *Traf6* in murine HSPC recapitulates the hematologic features of del(5q) MDS in a transplant model (10), providing convincing evidence that sustained TLR activation is a critical factor driving the malignant phenotype. More recent findings indicate that *TRAF6* is essential for survival and proliferation of MDS HSPC (11) and sustained TLR activation skews their commitment toward the myeloid lineage while suppressing osteoblast differentiation (12, 13), analogous to the senescence-dependent changes observed with normal aging (14).

Immature myeloid-derived suppressor cells (MDSC), known to accumulate in tumor-bearing mice and cancer patients, are site-specific inflammatory and T cell immunosuppressive effector cells that contribute to cancer progression (15, 16). Their suppressive activity is in part driven by inflammation-associated signaling molecules, such as the danger-associated molecular pattern (DAMP) heterodimer S100A8/S100A9 (also known as myeloid-related protein 8 [MRP-8] and MRP-14, respectively), which interact with several innate immune receptors that are involved in the biology of MDSC activation (17–20). Murine CD11b⁺Gr1⁺ MDSC form the basis of the vast majority of the mechanistic studies; however, much less has been reported on their human counterparts. Human MDSC lack most markers of mature immune cells (LIN⁻, HLA-DR⁻) but possess CD33, the prototypical member of sialic acid-binding Ig-like super-family of lectins (Siglec) (15, 21–23). Importantly, while its precise action is unknown, CD33 possesses an immunoreceptor tyrosine-based inhibition motif (ITIM) that is associated with immune suppression (23).

Authorship note: Xianghong Chen, Erika A. Eksioglu, and Junmin Zhou contributed equally to this work. Dmitry I. Gabrilovich, Alan List, and Sheng Wei share are co-senior authors.

Conflict of interest: The authors have declared that no conflict of interest exists.

Citation for this article: *J Clin Invest.* 2013;123(11):4595–4611. doi:10.1172/JCI67580.

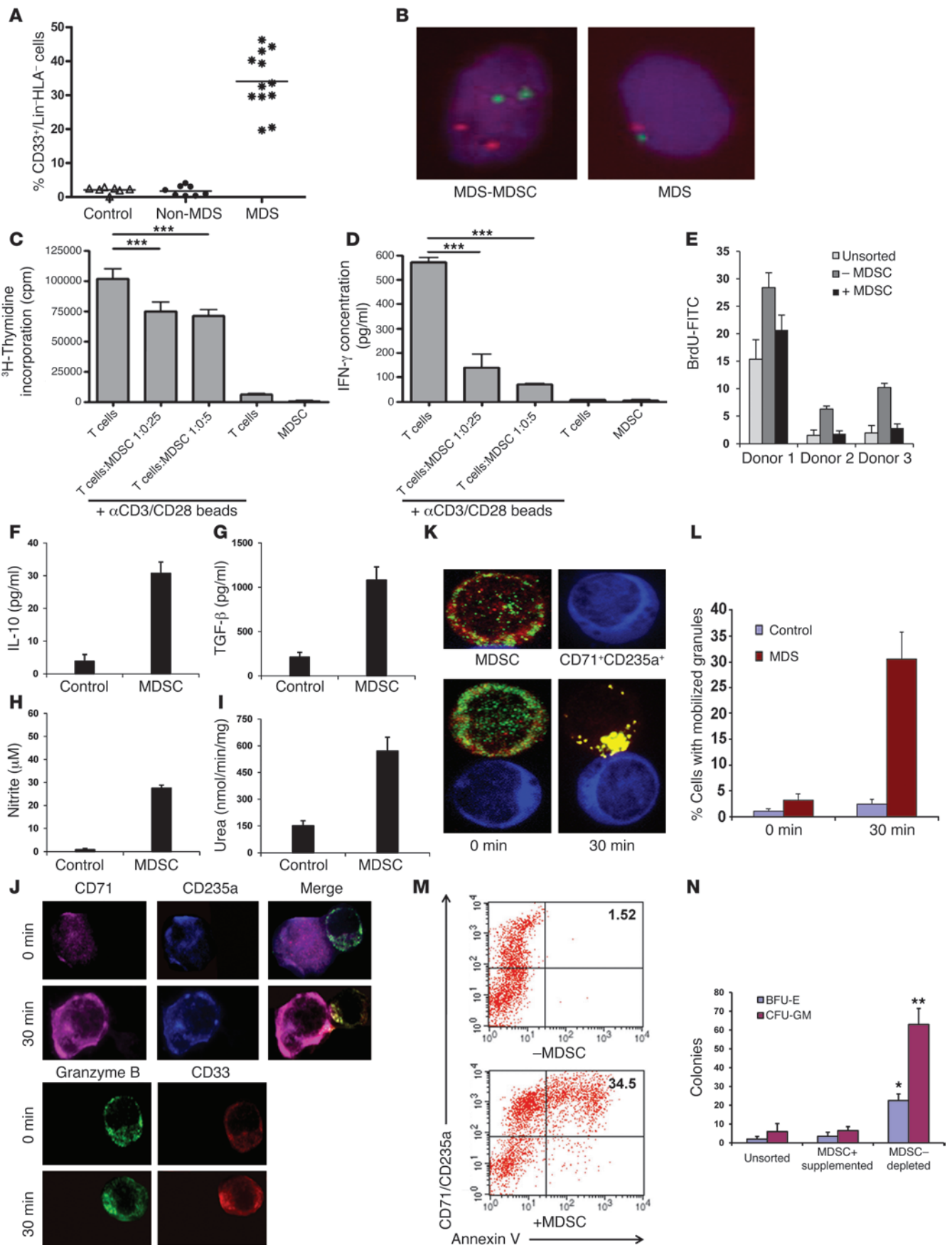




Figure 1

Increased accumulation and function of MDSC in BM of MDS patients. (A) Percentage of MDSC in the BM-MNC of MDS ($n = 12$), age-matched healthy ($n = 8$), and non-MDS cancer specimens ($n = 8$, $P < 0.0001$). (B) Chromosome 7 FISH of sorted MDSC or non-MDSC from MDS BM-MNC ($n = 5$, CEP7 is green and 7q31 orange). ^3H -thymidine incorporation (C) and IFN- γ ELISA (D) of stimulated autologous T cells cocultured with sorted MDS-MDSC at 1:0.25 and 1:0.5 ratios (T cells:MDSC). Error bars denote SD of 3 separate patient samples tested in triplicate. (E) BrdU incorporation of stimulated T cells after admixing with autologous unsorted, MDSC depleted (–MDSC), or remixed (+MDSC) BM-MNC. Sorted MDSC from MDS or healthy donor BM tested for IL-10 (F), TGF- β (G), NO (H), and arginase (I) production after 24 hours of culture. (J) MDSC/erythroid precursor contact zone of admixed sorted MDS-MDSC and autologous erythroid precursors at a ratio of 1:3 (MDSC/erythroid precursor) by microscopy at 0 and 30 minutes. Cells were stained for CD71 (pink), CD235a (blue), CD33 (red), and granzyme B (green). (K) Sorted MDSC from MDS or healthy donors labeled with CD33 (red) and granzyme B (green) coincubated with purified autologous erythroid precursors (0 or 30 minutes) and monitored by microscopy. (L) Counts of MDSC-HPC conjugate mobilized granules. Original magnification, $\times 400$ (B); $\times 600$ (J and K). (M) Annexin V exposure on erythroid precursors (CD71 $^+$ CD235a $^+$) incubated with or without sorted autologous MDS-MDSC. (N) Colony-forming ability of unsorted, –MDSC, or remixed (+MDSC) MDS BM-MNC (ratio of 1:3). * $P < 0.005$; ** $P < 0.001$; *** $P < 0.05$.

Here, we show that LIN $^+$ HLA-DR $^+$ CD33 $^+$ MDSC specifically accumulate in the BM of MDS patients (herein referred to as MDS-MDSC) and impair hematopoiesis through a mechanism that involves S100A9 as an endogenous ligand for CD33-initiated signaling. Importantly, using S100A9 transgenic (S100A9Tg) mice, we show that sustained activation of this inflammatory pathway leads to the development of MDS and that this hematologic phenotype is rescued by strategies that suppress CD33 ITIM signaling. Our finding that S100A9 ligates CD33 to induce MDSC expansion suggests that targeting this pathway may provide a therapeutic approach for the treatment of MDS. Finally, the discovery of this signaling pathway verifies the role of S100A9 as an important initiator of immune suppression. S100A9Tg mice may therefore serve as a useful model for the study of MDS pathogenesis, treatment, and the overall role of MDSC in cancer.

Results

Lin $^+$ HLA-DR $^+$ CD33 $^+$ MDSC are expanded in MDS primary BM specimens and direct the suppression of autologous erythroid precursors. BM mononuclear cells (BM-MNC) were isolated from MDS BM aspirates ($n = 12$), age-matched healthy BM ($n = 8$), or non-MDS cancer patients (4 breast and 4 lymphoma) and analyzed for the presence of LIN $^+$ HLA-DR $^+$ CD33 $^+$ MDSC by flow cytometry. MDS patients exhibited markedly higher numbers of MDSC (median 35.5%, $P < 0.0001$) compared with healthy donors or non-MDS cancer patients (less than 5%, Figure 1A). To determine whether MDS-MDSC are derived from the malignant MDS clone, LIN $^+$ HLA-DR $^+$ CD33 $^+$ MDSC were sorted from MDS specimens with chromosome 5q [del(5q)] or 7q [del(7q)] deletion and analyzed by FISH with specific probes. Cytogenetically abnormal cells harboring del(5q) or del(7q) were restricted to the non-MDSC population, whereas LIN $^+$ HLA-DR $^+$ CD33 $^+$ MDSC displayed a correspondingly normal chromosome complement (Figure 1B). Exome sequencing studies have shown that clonal somatic gene mutations are demonstrable in the vast majority of MDS specimens lacking chro-

mosome abnormalities by metaphase karyotyping. To further evaluate the relationship between MDS-MDSC and the MDS clone, we performed a quantitative PCR (qPCR) array of the most common gene mutations in MDS (QIAGEN) in purified MDS-MDSC and non-MDSC populations from primary BM MDS specimens. Mutations involving *CBL*, *EZH2*, *IDH1/2*, *N-RAS*, *SRSF2*, *U2A535*, and *RUNX1* genes were detected in the MDS specimens; however, all mutations were restricted to the MDSC-depleted fraction (Supplemental Table 1; supplemental material available online with this article; doi:10.1172/JCI67580DS1), indicating that LIN $^+$ HLA-DR $^+$ CD33 $^+$ MDSC are distinct from the malignant clone.

Recognized functional properties of MDSC include suppression of antigen-stimulated or CD3-stimulated T cell proliferation and IFN- γ production (15, 24). T cells purified from the BM of MDS patients showed reduced T cell proliferation (Figure 1C) and IFN- γ production (Figure 1D) after coculture with autologous MDS-MDSC, demonstrating the expected suppressive activity of these cells. To further validate these findings, we depleted MDSC from MDS BM specimens prior to anti-CD3/anti-CD28 stimulation and then added the MDSC back to the control group. MDSC depletion significantly improved T cell responses compared with the MDSC-supplemented group (Figure 1E), thereby linking the observed impaired T cell responsiveness to the actions of BM-derived MDSC. In addition, suppressive MDS-MDSC overproduced suppressive cytokines such as IL-10 and TGF- β (Figure 1, F and G) as well as nitric oxide (NO) and arginase compared with LIN $^+$ HLA-DR $^+$ CD33 $^+$ cells isolated from healthy donors (Figure 1, H and I). Collectively, these data demonstrate that LIN $^+$ HLA-DR $^+$ CD33 $^+$ MDSC are a unique and functional cellular subset supporting a proinflammatory microenvironment and immune tolerance in the BM of MDS patients.

MDSC-mediated suppressive and cytotoxic effector functions require direct contact with target cells. One mechanism utilized by cytotoxic effectors is the mobilization of pore-forming granules and the release of caspase-activating effector proteases, such as granzyme B, to the site of effector/target contact, which induces apoptosis of the target cell (25). Since MDSC reside in close proximity with hematopoietic progenitor cells (HPC), which in MDS display an increased apoptotic rate, we tested whether MDSC-mediated cytostatic activity may contribute to HPC death. To address this, we examined MDS-MDSC granule mobilization and release of granzyme B using 4-color immunofluorescence staining. MDS-MDSC exhibited strong granzyme B polarization at the site of cell contact with CD235a $^+$ (glycophorin A)/CD71 $^+$ autologous erythroid precursors (Figure 1J). After 30 minutes incubation, the frequency of such effector/target conjugates in MDS patient specimens was significantly higher (34%) than in samples from healthy donors (5% $P < 0.001$, Figure 1, K and L). These cellular interactions resulted in apoptosis of targeted erythroid precursors (Figure 1M), demonstrating that in addition to known MDSC-mediated immune suppressive functions, there is an unrecognized MDSC-mediated hematopoietic suppressive capacity. To corroborate this finding, we examined the effects of MDSC on the proliferative capacity of HSPC in MDS-MDSC-depleted, HSPC-enriched BM patient specimens in a methylcellulose colony formation assay. Burst-forming unit–erythroid (BFU-E) and GM-CFU colony formation were significantly higher in MDSC-depleted specimens compared with both MDSC-supplemented and unsorted samples (Figure 1N), demonstrating that MDSC have a direct suppressive role on erythroid and myeloid progenitor cell development.

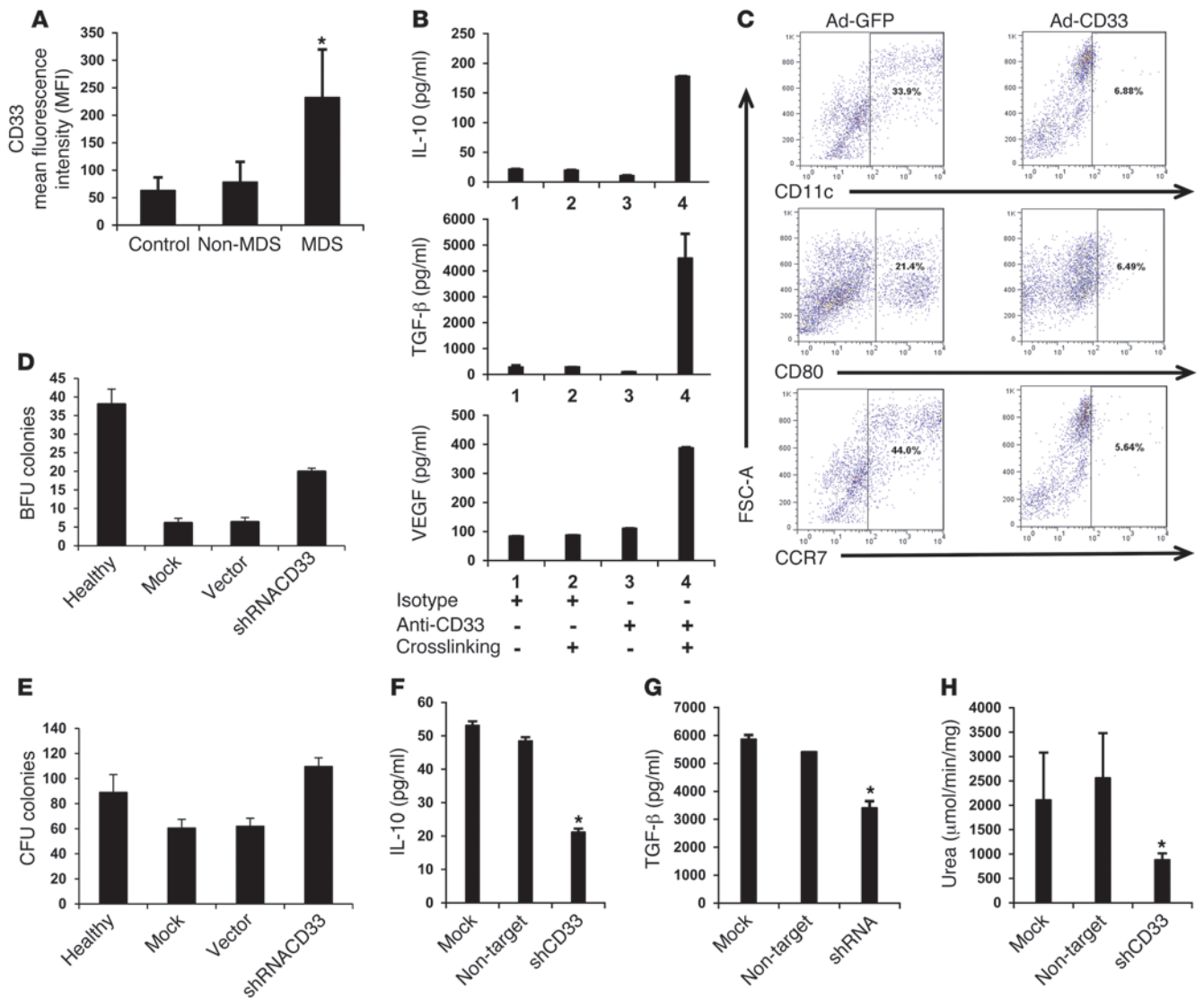


Figure 2

CD33 signals to enhance MDSC suppressive functions. (A) BM-MNC from MDS patients ($n = 12$), age-matched healthy donors ($n = 8$), and non-MDS cancers ($n = 8$) were analyzed for CD33's MFI. $*P < 0.0005$. (B) Concentration of IL-10, TGF- β , and VEGF from the supernatant of CD33 (or isotype) crosslinked U937 cells. Bars represent mean \pm SEM of 3 wells on 3 separate experiments. (C) BM-MNC were isolated from healthy donors and infected with an adenoviral vector containing either GFP (Ad-GFP) or CD33 (Ad-CD33) for 72 hours before flow cytometric analysis of the mature myeloid markers, CD11c, CD80, and CCR7, with noninfected cells as a control (data not shown). (D) BFU and (E) CFU colony-forming assay. After sorting out MDSC from the BM of MDS patients, the remaining MDSC-negative cells were cultured with MDSC that had been mock infected or infected with LV containing nontargeted shRNA or CD33 shRNA (shCD33) for 14 days. The colony formation assay was performed. The MDSC were also cultured for 72 hours after infection with LV containing constructs described above before culturing with MDSC-negative BM cells. $*P < 0.001$, versus cells treated with control shRNA. The supernatants were collected and assayed for IL-10 (F) and TGF- β (G) by ELISA. $*P < 0.05$, versus cells treated with control shRNA. (H) The shCD33-treated cells were also analyzed for arginase activity. $*P < 0.05$, versus cells treated with control shRNA.

Increased CD33 expression and signaling contribute to MDSC suppressive functions and hematopoietic impairment. MDSC in humans characteristically express the surface transmembrane glycoprotein CD33, a Siglec 3 receptor that along with other members of this family, has prominent roles in inflammation (23, 26–35). However, the involvement of CD33 in myelopoiesis remains unexplored. Hence, we investigated the relationship between CD33 membrane expression density on MDS-MDSC and its activation and maintenance in MDS BM. We found that these

cells robustly express CD33 at levels higher than LIN-HLA-DR-CD33⁺ cells isolated from non-MDS-associated cancer patients and healthy donor BM cells (Figure 2A). To explore the functional consequences of CD33 engagement, we crosslinked CD33 in U937 cells (a human monocytic cell line with high CD33 expression), which triggered IL-10, TGF- β , and VEGF secretion (Figure 2B). To examine whether CD33 can promote MDSC accumulation and/or activation, we overexpressed CD33 with an adenovirus vector in BM-MNC from healthy donors, which



significantly suppressed myeloid cell development, as evidenced by reduced expression of the maturation markers CD11c, CD80, and CCR7 (Figure 2C). To further establish the role of CD33 in MDSC-mediated BM suppression, we knocked down CD33 in MDS-MDSC using a lentiviral vector (LV) containing CD33-specific shRNA. Coculture of autologous HSPC with CD33 shRNA-treated MDS-MDSC resulted in a 2- to 3-fold increase in BFU-E and GM-CFU colony recovery compared with those cultured with scrambled shRNA-treated and nontransduced MDS-MDSC and healthy donor BM MDSC (Figure 2, D and E). Moreover, production of IL-10, TGF- β , and arginase was reduced in CD33 shRNA-treated MDS-MDSC compared with control cells (Figure 2, F-H). Collectively, these data delineate a role for CD33 in MDSC activation and expansion in MDS and directing hematopoietic impairment.

S100A9 is a native ligand for CD33. Although our investigations show that CD33/Siglec 3 is a key receptor involved in functional activation of MDSC, its native ligand remains unknown. Therefore, we attempted to identify potential ligand(s) for this receptor by creating a chimeric fusion protein with the ectodomain of CD33 and the Fc portion of human IgG (hereafter referred to as CD33-fusion). BM cell lysates from MDS patients were immunoprecipitated with the CD33-fusion followed by high-throughput mass-spectrometric analysis on associated peptides. S100A9, an inflammatory signaling molecule known to activate MDSC, was among the most prominent protein bands identified (Figure 3A). To confirm the specificity of the binding of this DAMP to CD33, we prepared both S100A8 and S100A9 transfectants in the rhabdomyosarcoma cell line SJCRH30, which lacks detectable expression of endogenous CD33 or S100A9. The CD33-fusion (APC) stained only S100A9 transfectant cells, but not S100A8 transfectant cells, confirming binding specificity (Figure 3B; transfectants were stained with FITC, and specific binding by the CD33-fusion was stained with APC, shown in red; nuclei were stained with DAPI). Direct binding of S100A9 to CD33 was confirmed further in a sandwich ELISA where the capture antibody was anti-S100A9 (Figure 3C) as well as by dot blot analysis of transfectant cell lysates with CD33-fusion (Figure 3D), demonstrating the specificity of the interaction. To fully corroborate the binding of this pair, we set out to perform a reverse immunoprecipitation on CD33 transfectant cells showing that S100A9 coprecipitated with CD33 only in recombinant human S100A9-treated (rhS100A9-treated) cells (Figure 3E). To validate clinically the ligand specificity in MDS patients, we compared the pull-down with CD33-fusion from PBMC and BM from healthy as well as MDS patients' samples. As expected, the highest amount of S100A9 was precipitated from the BM of MDS patient specimens (Figure 3F). Next, to understand the kinetics of S100A9 and CD33 interactions, SJCRH30 cells were transfected with either vector or CD33 and incubated with rhS100A9 tagged with DDK (DYKDDDDK epitope, same epitope as Flag). We observed a time-dependent increase in binding of rhS100A9 to stable SJCRH30-CD33 cells but no binding to vector transfected cells (Figure 3G). To demonstrate the functionality of this ligation pair, we added rhS100A9 to SJCRH30-CD33 cells, which triggered CD33-mediated upregulation of IL-10 and TGF- β expression (Figure 3, H and I). To confirm that rhS100A9 can recapitulate our observation of the secretion of these cytokines after crosslinking CD33, we repeated the experiments in U937 cells with rhS100A9 and again found an increase in production of both cytokines (Figure 3, J and K). Importantly,

BM plasma concentration of S100A9 was significantly increased in MDS patients compared with BM plasma from healthy donors (Figure 3L). Moreover, the engagement of CD33 with rhS100A9 in MDS-MDSC from patient BM resulted in a time-dependent colocalization of this ligand/receptor pair (Figure 3M). It is well recognized that CD33 signals through phosphorylation of ITIMs that recruit Src homology region 2 domain-containing phosphatase-1 (SHP-1) (31). rhS100A9 ligation correspondingly increased the recruitment of SHP-1, confirming that CD33 signals through its ITIM after S100A9 ligation in MDS BM (Figure 3N). In addition, directly treating CD33-transfected SJCRH30 with the BM plasma of MDS patients triggered the recruitment of SHP-1 to ITIM when compared with cells treated with the plasma of healthy donors, suggesting that increased secretion of S100A9 in the local BM microenvironment may have a role in the activation of CD33-ITIM signaling (Figure 3O).

S100A8/S100A9 engagement of CD33 triggers MDS-MDSC activation. Having established S100A9 and CD33 as a functional ligand/receptor pair, we explored the role of this interaction in replicating the functional responses observed with receptor crosslinking. We again induced CD33 overexpression in healthy BM cells through adenovirus transfection and studied their immunosuppressive properties with or without the addition of rhS100A9. Forced expression of CD33 induced a parallel increase in gene expression and secretion of the suppressive cytokines IL-10 and TGF- β (Figure 4, A-D), which was greatly increased by the addition of rhS100A9. Secretion of the suppressive cytokine TGF- β was only observed after rhS100A9 treatment of CD33 transfectant cells (Figure 4D), accompanied by an increase in the expression of NOS2 and ARG2, consistent with the suppressive cytokine profile (Figure 4, E and F). Figure 4, G and H, demonstrates the transfection efficiency of the CD33 adenovirus at both the gene and protein expression levels measured by qPCR and GFP by flow cytometry, respectively.

To further delineate the specific role of S100A9's ligation with CD33 compared with its other ligands, we blocked RAGE, TLR4, and CD33 as well as their combination with antibodies before treating healthy BM cells with rhS100A9. As expected, rhS100A9 treatment is able to induce the generation of suppressive cytokines as compared with untreated cells. Importantly, our data show that blockade of CD33 reduced both IL-10 and TGF- β production (Figure 4, I and J), while treatment with anti-RAGE and anti-TLR4 had no significant effects on IL-10 production but displayed modest suppression of TGF- β secretion and expression (Figure 4, I and J). These findings suggest that although CD33 plays a critical role in the secretion of both cytokines, we cannot completely exclude the contribution of other receptors associated with local BM inflammation. To confirm that S100A9 expression contributes to inflammation in the BM microenvironment, we knocked down S100A8 and S100A9 in MDS-MDSC using gene-specific shRNAs (Figure 4K). Given that S100A9 usually pairs with S100A8 as a heterodimer and both are concomitantly regulated, we were not surprised to find reciprocal changes in gene expression after downregulation in the expression of the alternate protein (36). Importantly, reduction of S100A8/S100A9 expression profoundly attenuated IL-10 and TGF- β production (Figure 4, L and M) and rescued autologous BFU-E and GM-CFU colony formation (Figure 4N). These data show that inflammation-associated S100A8/S100A9 signaling plays a critical role in the activation of MDS-MDSC and suppresses normal hematopoiesis.

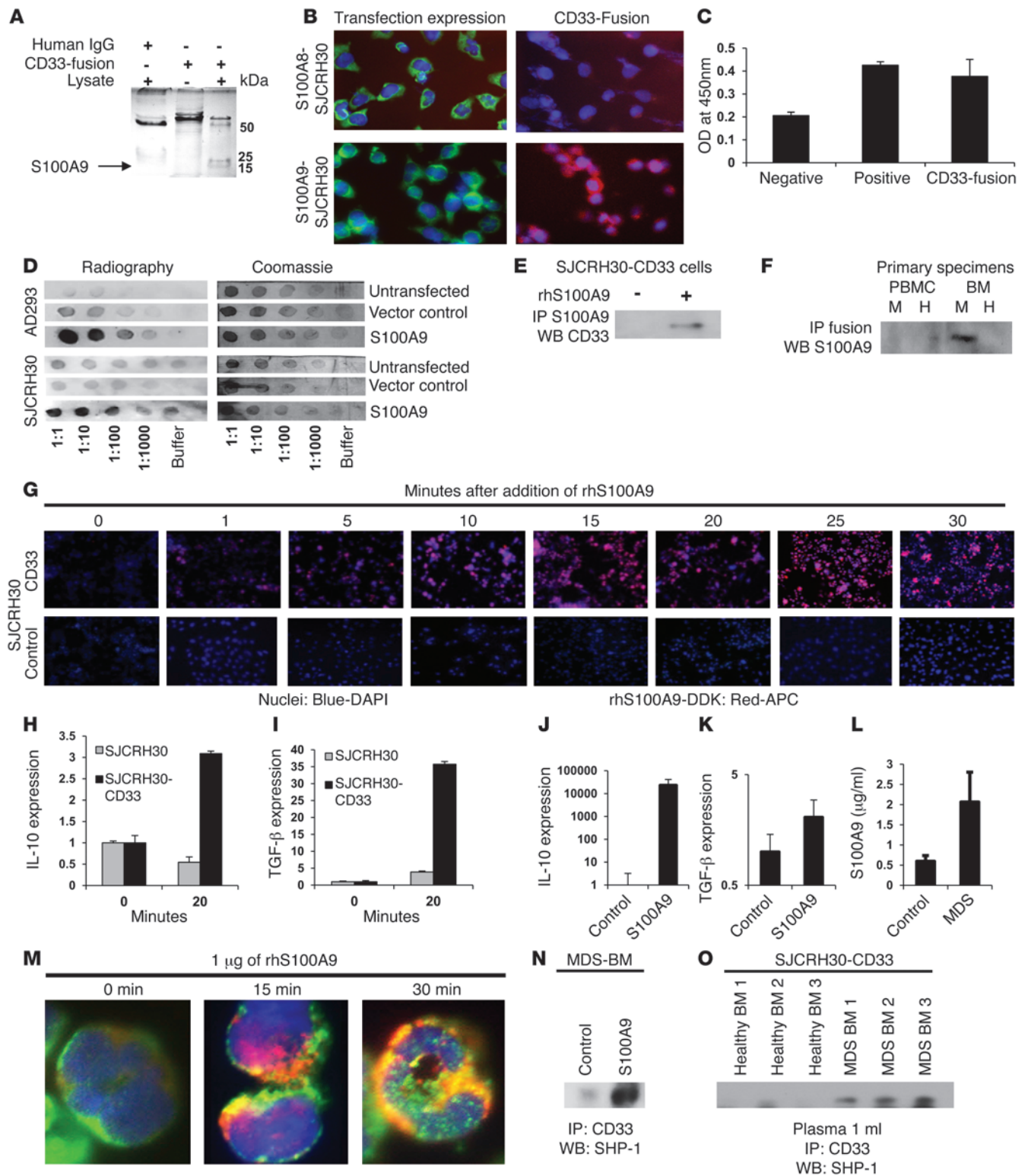




Figure 3

Identification of S100A9 as a native ligand for CD33. (A) Coomassie blue staining of BM lysates precipitated with either control IgG or CD33-fusion. (B) Transfected SJCRH30 cells (S100A8 on top left and S100A9 lower left) stained with CD33-fusion (APC, red). (C) S100A9 capture-ELISA of lysates from untransfected (negative) or S100A9 transfected cells. Secondary antibody was either anti-S100A9 (positive control) or CD33-fusion. (D) Serial dilution of both AD293 and SJCRH30 cell lysates, either untransfected or transfected with vector or S100A9, onto a PVDF membrane and blotted with CD33-fusion. Coomassie blue staining serves as loading control. (E) S100A9 immunoprecipitation of SJCRH30 CD33/S100A9 cotransfected cell lysate blotted against CD33. (F) PBMC and BM-MNC from healthy (H) and MDS (M) samples immunoprecipitated with CD33-fusion and blotted for S100A9. (G) Immunofluorescence staining of rhS100A9-DDK incubated with either CD33-transfected (top) or vector-transfected (bottom) SJCRH30 cells at indicated time points. DAPI = nuclei, APC-DDK = rhS100A9. Treatment of SJCRH30-CD33 cells with rhS100A9 induced IL-10 (H) and TGF- β expression (I). Treatment of U937 cells (high CD33 expression myeloid cell line) with rhS100A9 also induced IL-10 (J) and TGF- β expression (K). S100A9 protein concentration in the plasma of MDS patients ($n = 6$) measured by ELISA (L). MDS-MDCS treated with 1 μ g of rhS100A9 were stained for CD33-FITC and anti-DDK-APC (M) and immunoprecipitated with anti-CD33 antibody followed by blotting with anti-SHP-1 (N). Original magnification, $\times 400$ (B); $\times 200$ (G); $\times 600$ (M). (O) BM plasma from either healthy donors ($n = 3$) or MDS patients ($n = 3$) was used to assay SHP-1 recruitment. In all experiments, error bars represent the SEM of 3 separate experiments.

S100A9Tg mice recapitulate features of human MDS. Given our findings that S100A9 triggers CD33/Siglec 3 signaling and is involved in MDSC activation (17, 18, 37), we generated S100A9Tg mice to study MDSC-associated inflammation (37). Since MDS is an age-associated disease, we began by analyzing changes in the proportion of BM Gr1⁺CD11b⁺ cells (cells with MDSC-phenotype, hereafter also referred to as MDSC) with age in S100A9Tg compared with S100A9 knockout (S100A9KO) (38) or WT mice at 6, 18, or 24 weeks of age. We observed a marked age-dependent accumulation of MDSC in the BM of S100A9Tg mice, but not in S100A9KO or WT mice, that reached its maximum by 18 weeks and was maintained into 24 weeks of age (Figure 5A). Similarly, the proportion of MDSC in PBMC and spleen also increased with age (Figure 5B). Although changes in the proportion of MDSC in the spleen were comparatively less than in the BM, it was accompanied by a decrease in the proportion of mature cells (Figure 5, C and D), effectively increasing the ratio of immature to mature cells in this hematopoietic organ. Functionally, only the MDSC from 24-week-old S100A9Tg mice, but not S100A9KO or WT mice, significantly inhibited BFU-E (Figure 5E) and GM-CFU formation (data not shown), which was rescued after depletion of MDSC in the S100A9Tg group (Figure 5E). Importantly, as further evidence of the role of S100A9 as an essential inflammatory factor regulating MDSC expansion and suppressive activity, IL-10 and TGF- β secretion were significantly increased in S100A9Tg mice compared with KO or WT animals (Figure 5F).

To evaluate the *in vivo* consequences of S100A9 overexpression on hematopoiesis, serial complete blood counts (CBC) were analyzed from WT and S100A9Tg mice at 6, 18, and 24 weeks of age. S100A9Tg mice developed progressive multilineage cytopenias characterized by decreasing hemoglobin (Hgb), rbc number, neutrophil and platelet counts evident as early as 6 weeks of age. By 18 weeks, S100A9Tg mice exhibited severe anemia and thrombo-

cytopenia with a greater than 22.0% decrease in rbc, 20.1% decrease in Hgb, and 77.8% decrease in platelets (Table 1). By 24 weeks of age, S100A9Tg mice developed severe pancytopenia. Histological examination of BM aspirates and biopsy sections from WT mice displayed normal morphology and cytological features (Figure 5, G–J). In contrast, the BM of S100A9Tg mice was hypercellular (95% cellularity), accompanied by tri-lineage cytological dysplasia (Figure 5, K–N). Megakaryocyte morphology recapitulated the dysplastic features characteristic of human MDS, with a preponderance of mononuclear or hypolobated forms. Erythroid precursors displayed megaloblastoid maturation with abnormal hemoglobinization and occasional binucleation. Nuclear budding and bizarre mitotic forms were also apparent (Figure 5, K–N). The percentage of myeloid lineage cells identified by myeloperoxidase staining increased significantly in S100A9Tg mice, reaching a mean of $62.5\% \pm 5.6\%$ vs. $35\% \pm 10\%$ in WT mice ($P = 0.0099$). Assessment of distribution of cycling cells by Ki67 staining showed a marked increase in the proportion of Ki67⁺ cells in the endosteal region of S100A9Tg mice compared with WT mice (mean, $78.5\% \pm 6.1\%$ vs. $37.5\% \pm 3.7\%$; $P = 0.0013$), whereas there was no discernible difference in the central marrow region (mean Tg, 9.75 ± 0.77 vs. WT, 10 ± 2.04 ; $P = 0.62$, Supplemental Figure 1).

Although this model closely replicates the inflammatory milieu observed in human MDS, HSPC from S100A9Tg mice also express the S100A9 protein. Given that the provenance of this protein in human MDS is unknown, we investigated cellular expression of S100A9 in MDS BM-MNC by flow cytometry. S100A9 intracellular staining was detected in CD33⁺ cells, whereas CD34⁺ HSPC had no demonstrable S100A9 expression (Figure 5, O and P). We did not detect S100A9 expression in other immune cells, such as CD3⁺ lymphocytes, CD19⁺ B cells, or CD56⁺ NK cells (data not shown).

Analysis of the role of MDSC by adoptive transfer of enriched HSPC from S100A9Tg mice. To more accurately delineate the role of MDSC from S100A9Tg mice in hematopoiesis, we performed competitive adoptive transfer of enriched HSPC into lethally irradiated (900 cGy) female FVB/NJ mice with age-matched WT HSPC, S100A9Tg HSPC, or an admixture (1:1 ratio) of enriched BM HSPC from male mice. When we used a male-to-female SRY gene expression PCR approach to monitor engraftment (39, 40), all mice experienced around 90% engraftment (Supplemental Figure 2). After engraftment (defined as $wbc > 3 \times 10^3$ cells/ μ l in WT recipients at 8 weeks), recipients of WT HSPC had proportions of both BM-derived Gr1⁺CD11b⁺ and KLS stem cells (Figure 6, A and C) that were comparable to levels in untransplanted WT mice (Figure 5A). In contrast, adoptive transfer with S100A9Tg enriched HSPC generated a high proportion of GFP-expressing Gr1⁺CD11b⁺ MDSC (Figure 6B) accompanied by a reduced proportion of HSPC, findings analogous to our observations in older transgenic mice (Figure 6C). However, mice that received the admixed HSPC population had a proportion of MDSC approaching that in WT adoptively transferred mice (~30%). Notably, nearly 50% of MDSC lacked GFP expression, indicating origination from WT HSPC (Figure 6B), whereas the remaining GFP⁺ MDSC derived from S100A9Tg donor cells. Although the total MDSC population did not increase to the level observed in the S100A9Tg adoptively transferred mice, we observed a decreased proportion of HSPC to levels found in mice transplanted with S100A9Tg donor cells (Figure 6C). These findings indicate that the smaller population of activated MDSC from S100A9Tg donor cells had sufficient suppressive activity to

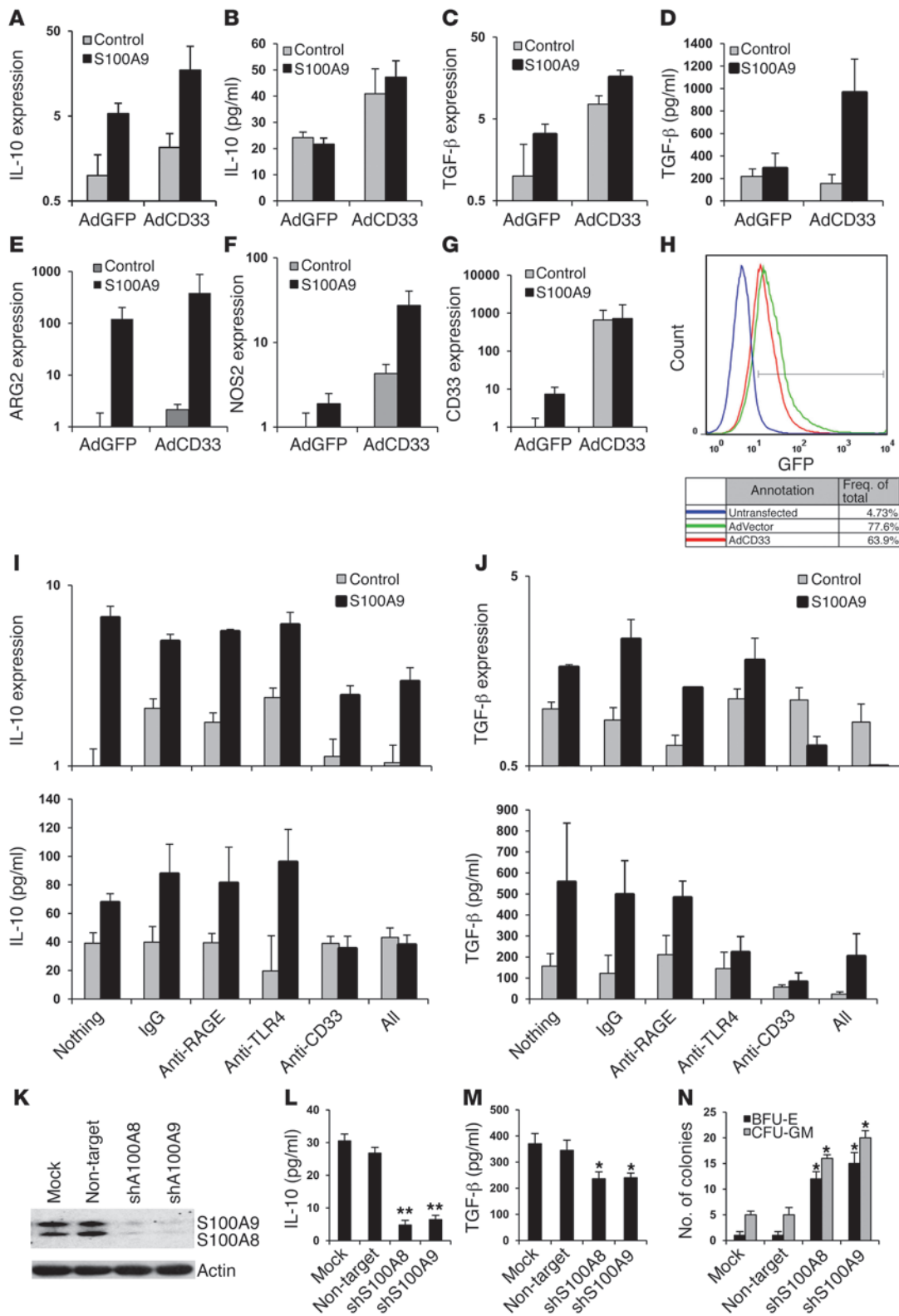




Figure 4

S100A9 signaling through CD33 in MDS BM is associated with MDSC activation and suppressive function. Healthy BM cells infected with adenovirus containing GFP or CD33 expression vectors assessed by qPCR for the expression of IL-10 (A), TGF- β (C), ARG2 (E), or NOS2 (F), or by ELISA for IL-10 (B) and TGF- β (D). qPCR (G) and flow cytometry of GFP expression (H) determined transfection efficiency. Healthy BM cells' RAGE, TLR4, CD33, or their combination were blocked prior to culturing cells by themselves or with 1 μ g of S100A9 for 48 hours to determine IL-10 gene and protein expression (qPCR in the top and ELISA on the bottom) (I) or TGF- β gene and protein expression (J). (K) Silencing S100A8 and S100A9 expression in primary MDS-BM cells using specific shRNA (demonstrated by Western blot) inhibits the expression of IL-10 (L) and TGF- β (M). * P < 0.01; ** P < 0.001, versus cells treated with control shRNA. (N) Blocking S100A8 and S100A9 expression by specific shRNA promotes colony formation in BM cells isolated from patients with MDS. * P < 0.05, versus cells treated with control shRNA. In all experiments, error bars represent the SEM of triplicate determination with 3 separate primary specimens.

yield a comparable impairment of hematopoietic integrity. These findings were supported by sequential analyses of peripheral blood counts in which mixed source transplant recipients had cytopenias that were intermediate in severity relative to those in mice receiving the S100A9Tg or WT donor cells (Figure 6, D–F). Interestingly, while mixed donor recipients had the same proportion of HSPC after engraftment as Tg transplanted mice, their wbc counts were higher than those of mice transplanted with S100A9Tg HSPC and lower than the levels found in WT HSPC recipients. Similarly, onset of anemia was delayed in recipients of the mixed versus S100A9Tg donor cells, eventually matching the proportion of KLS HSPC in mixed versus transgenic mice at the end of the study (8 weeks, as shown in Figure 6C). These findings suggest that normal HSPC from WT mice are able to partially rescue hematopoiesis but, with time, it is suppressed by accumulating MDSC derived from S100A9Tg donor cells.

To address whether S100A9 alone has direct effects on HSPC, we treated BM CD34⁺ (MDSC depleted, MDSC⁻) from MDS patient specimens with rhS100A9 for 24 and 48 hours and assessed apoptosis by flow cytometry. We observed a decrease in the number of CD34⁺ HSPC after treatment compared with controls accompanied by a corresponding increase in the apoptotic fraction among surviving cells after 48 hours of exposure (Figure 6, G and H, and refs. 41–43). In order to corroborate these findings, we cultured healthy BM-derived CD34⁺ cells (Lonza) with rhS100A9 and again observed a decrease in viable cells after treatment (50.7% viability in control cells versus 24.7% in rhS100A9-treated cells, Figure 6I). These findings suggest that S100A9 has a direct apoptotic effect in human HSPC.

Forced maturation of MDSC restores hematopoiesis. To confirm the effector role of MDSC and investigate the potential benefit of targeted suppression of MDSC, we treated S100A9Tg mice with *all-trans-retinoic acid* (ATRA). ATRA induces MDSC differentiation into mature myeloid cells and neutralizes ROS production, thereby extinguishing MDSC through forced terminal differentiation (44, 45). To this end, we examined whether ATRA would induce MDSC differentiation in S100A9Tg mice and improve hematopoiesis. S100A9Tg and WT mice were treated with ATRA (250 μ g/200 μ l) or vehicle control orally for 5 consecutive days. Two days after completion of the treatment, we found that ATRA reduced the total number of MDSC, while numbers in WT mice

remained at basal levels (Figure 7A). Reductions in MDSC numbers in S100A9Tg mice were coupled to an increase in mature cells following ATRA treatment (Figure 7B). Treatment of primary MDS BM specimens with ATRA also reduced *in vitro* MDSC accumulation (data not shown). Importantly, BM progenitor cultures from ATRA-treated S100A9Tg mice showed significantly improved BFU-E recovery compared with vehicle-treated controls (Figure 7C). Analysis of changes in peripheral blood counts showed that rbc, wbc, and platelet counts significantly increased compared with vehicle-treated controls (Figure 7D), indicating that terminal differentiation of MDSC can restore effective hematopoiesis.

Our investigations showed that MDSC employ CD33-associated ITIMs to inhibit their own cellular maturation (Figure 3, N and O). However, ITIM signals can be overridden by stimulatory immunoreceptor tyrosine-based activation motif-mediated (ITAM-mediated) signals (46, 47). Some CD33-related receptors, such as certain Siglecs, lack ITIMs and instead function as activating receptors. Mouse Siglec-H and human Siglec-14 have been shown to interact with DAP12 (26, 27, 48, 49), an ITAM-containing adaptor that can promote myeloid cell maturation (Supplemental Figure 3) and inhibit TLR activation (50). We compared the *DAP12* gene expression of purified MDS-MDSC ($n = 5$) to age-matched healthy donor MDSC ($n = 5$). *DAP12* mRNA was significantly lower in MDS-MDSC in all specimens tested (Figure 7E). We reasoned that overriding CD33-ITIM signaling via DAP12 would induce the differentiation of these immature myeloid cells and improve hematopoiesis. To test this hypothesis, we created a constitutively active form of DAP12, named P23, and transfected AD293 cells with GFP, WT-*DAP12*, or active-*DAP12* P23 viral vectors. Our results show that P23 binds Syk kinase and activates downstream signaling in transduced AD293 cells without external stimulation (Figure 7F). Furthermore, P23 promotes primary human DC maturation as demonstrated by upregulation of CD80, CD83, and CCR7 antigens (Supplemental Figure 4 and refs. 26, 27). Based on these findings, we examined whether P23 could induce the maturation of MDS-MDSC and thereby prevent or disrupt hematopoietic suppression. We analyzed expression of the human monocytic and granulocytic surface markers CD14 and CD15 after transfection since this change, from CD14^{-/low}D15⁺ to CD14⁺CD15⁺ following active DAP12, indicates a shift to the monocyte/macrophage lineage (51). We found that while WT-*DAP12* transfection alone was sufficient to induce upregulation of CD14 and CD15, P23 transfection induced even greater expression of both maturation markers (Figure 7G). Moreover, P23 promoted the maturation of primary MDS-MDSC, as demonstrated by upregulation of CD80, CD83, and CCR7 maturation markers (Figure 7H). Finally, we tested whether DAP12-mediated MDSC maturation relieved suppression of erythropoiesis. We purified MDS-MDSC from 7 MDS patients and infected them with control, WT-*DAP12*, or P23 LV constructs. To assess the suppressive function of the mature MDS-MDSC on hematopoiesis, colony-forming capacity was assessed after culture of infected cells with autologous, MDSC-depleted BM cells. P23-infected MDS-MDSC cocultures yielded significantly higher colony numbers than control viral vector or WT-*DAP12*-infected MDS-MDSC cocultures (Figure 7I). These findings indicate that DAP12 overrides CD33-associated ITIM signaling to stimulate MDSC maturation and reverses the suppressive effects on HPC colony-forming capacity.

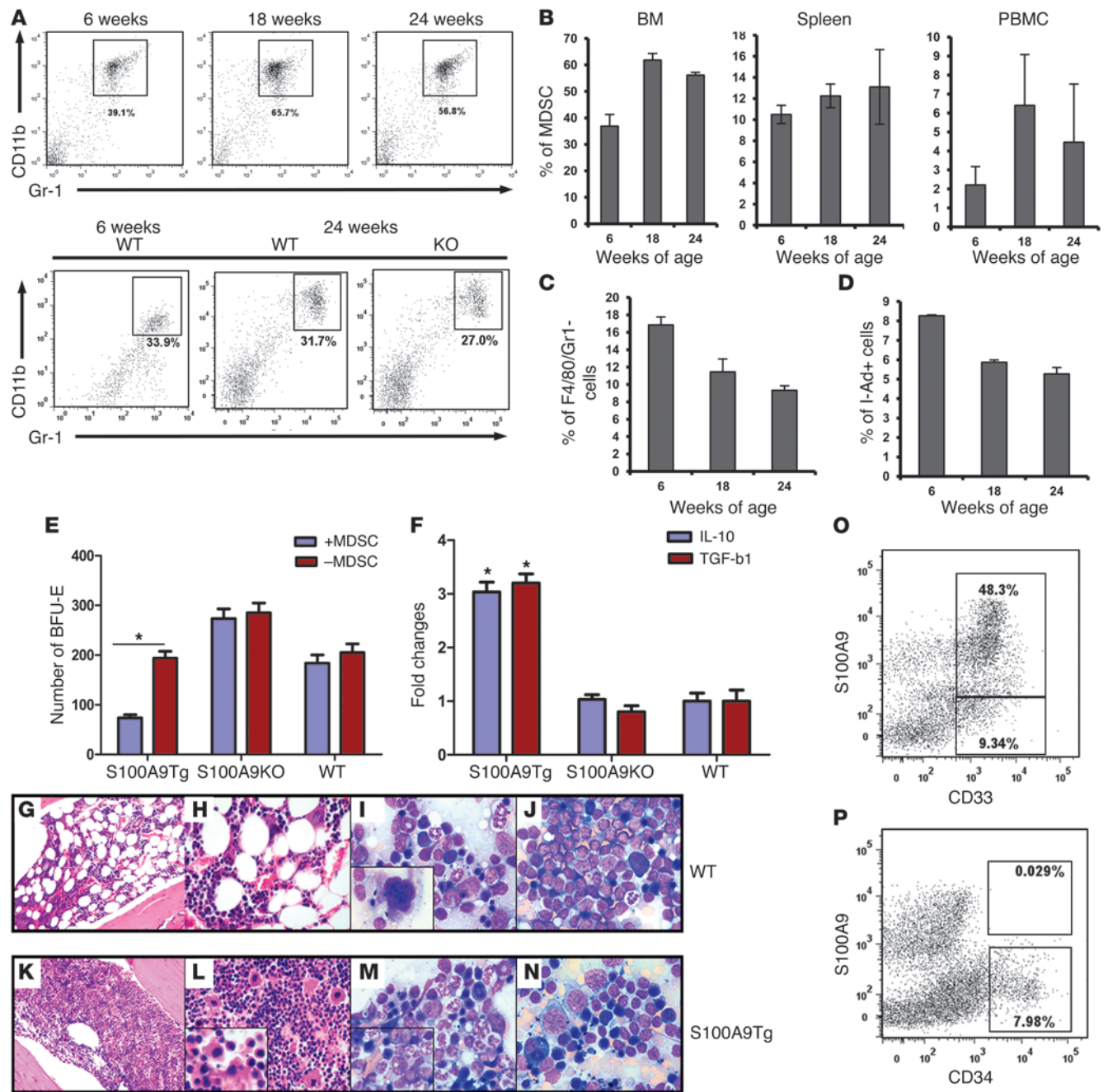


Figure 5

S100A9Tg mice have increased accumulation and activation of MDSC and display dysplastic features that recapitulate human MDS pathology. (A) Gr1⁺CD11b⁺ MDSC accumulation in BM-MNC isolated from S100A9Tg mice at 6, 18, or 24 weeks and S100A9KO or WT mice at both 6 and 24 weeks. (B) Percentage of MDSC from BM, spleen, and PBMC of S100A9Tg mice at 6, 18, and 24 weeks of age by flow cytometry. Spleen cells from B were also assayed against the maturation markers F4/80⁺Gr1⁻ (C) and I-Ad⁺ (D). (E) FACS-sorted Gr-1⁺CD11b⁺ cells (+MDSC) from the BM of mice described in A remixed back with autologous 1 × 10⁵ MDSC-negative population (containing HSPC, -MDSC) at 1:1 ratio for 14 days before evaluating colony formation. An MDSC-depleted population was used as the control. (F) MDSC from WT, S100A9Tg, and S100A9KO mice were FACS sorted and incubated in a 96-well plate for 24 hours after which IL-10 and TGF-β production were measured by ELISA. Comparison of the hematopathological analysis of WT (G–J) and S100A9Tg mice (K–N) Original magnification, ×200 (G and K); ×600 (H and L); ×1000 (J, I, M, and N). Detailed descriptions is in Methods. MDS-BM primary specimens were tested for the location of S100A9 in CD33⁺ cells (O) and CD34⁺ cells (P). Flow figures are representative of triplicate experiments.

**Table 1**
CBC of S100A9Tg and WT mice

Test	Units	6 weeks		18 weeks		24 weeks	
		WT	S100A9Tg	WT	S100A9Tg	WT	S100A9Tg
wbc	10 ³ /μl	5.4 ± 0.5	4.2 ± 1.5	6.0 ± 1.4	2.9 ± 0.2 ^A	6.3 ± 0.8	3.0 ± 0.4 ^A
LYM	10 ³ /μl	3.9 ± 0.5	2.6 ± 1.2	4.7 ± 1.1	2.4 ± 0.1 ^A	4.8 ± 0.7	2.5 ± 0.3 ^A
MONO	10 ³ /μl	0.4 ± 0.1	0.3 ± 0.2	0.4 ± 0.1	0.2 ± 0.1 ^A	0.4 ± 0.1	0.2 ± 0.1 ^A
GRAN	10 ³ /μl	1.1 ± 0.6	1.2 ± 1.2	0.9 ± 0.3	0.3 ± 0.2 ^A	1.1 ± 0.4	0.3 ± 0.1 ^B
HCT	%	48.1 ± 3.2	42.4 ± 2.1	45.7 ± 0.7	35.5 ± 3.0 ^B	45.4 ± 3.5	32.1 ± 2.7 ^B
MCV	fl	51.4 ± 1.6	49.8 ± 2.0	50.3 ± 0.5	50.0 ± 1.2	50.0 ± 1.3	50.0 ± 1.6
RDWa	fl	35.0 ± 0.7	33.2 ± 2.2	34.0 ± 1.3	32.5 ± 1.7	33.3 ± 1.4	32.2 ± 1.5
RDW	%	16.3 ± 0.7	15.9 ± 0.1	16.3 ± 0.5	15.5 ± 0.5	16.0 ± 0.5	15.4 ± 0.6
Hgb	g/dl	14.2 ± 0.8	13.0 ± 0.7	13.9 ± 0.3	11.1 ± 0.7 ^B	13.7 ± 0.6	10.3 ± 0.5 ^B
MCHC	g/dl	29.5 ± 1.1	30.6 ± 1.3	30.4 ± 0.4	31.5 ± 0.9	30.3 ± 1.0	32.3 ± 1.1
MCH	pg	15.1 ± 0.3	15.2 ± 0.1	15.3 ± 0.1	15.8 ± 0.3	15.2 ± 0.2	16.2 ± 0.4
rbc	10 ⁶ /μl	9.4 ± 0.7	8.5 ± 0.4	9.1 ± 0.1	7.1 ± 0.6 ^B	9.1 ± 0.3	6.4 ± 0.2 ^C
PLT	10 ³ /μl	555.7 ± 96.6	412.0 ± 124.0	431.3 ± 33.9	95.7 ± 35.0 ^C	437.0 ± 41.9	61.0 ± 23.5 ^C

All data are mean ± SEM ($n = 5$ mice). Peripheral blood samples were prepared from both S100A9Tg and control (WT) mice at the ages of 6, 18, and 24 weeks and analyzed on a Hema True Hematology Analyzer (Heska). ^A $P < 0.05$; ^B $P < 0.01$; ^C $P < 0.001$ vs. WT mice. LYM, lymphocytes; MONO, monocytes; GRAN, granulocytes; HCT, hematocrit; MCV, mean corpuscular volume; RDWa, rbc distribution with average; RDW, rbc distribution width; MCHC, mean corpuscular hemoglobin concentration; MCH, mean corpuscular hemoglobin; PLT, platelets.

Discussion

Inflammatory stimuli within the BM microenvironment are recognized as important biological signals stimulating progenitor cell proliferation and apoptosis in MDS. A recent population-based study extended this further by demonstrating a strong linkage between chronic immune stimulation and MDS predisposition (4). Definitive evidence that niche intrinsic abnormalities per se can alone account for development of MDS in a cell-nonautonomous fashion are limited. Raaijmakers and colleagues showed that selective osteoprogenitor dysfunction caused by deletion of *Dicer1* in the mesenchymal component of the BM microenvironment was sufficient to perturb hematopoiesis and lead to development of myeloid dysplasia, followed by secondary emergence of myeloid-restricted genetic abnormalities (52).

Our studies show that Lin⁺HLA-DR-CD33⁺ MDSC accumulate in the BM of MDS patients, derive from a population that is distinct from the neoplastic clone, and serve as cellular effectors that suppress hematopoiesis, promote T cell tolerance, and serve as a key source of myelosuppressive and inflammatory molecules such as IL-10, TGF- β , NO, and arginase. Using multiple biological and biochemical approaches, we show that S100A9 can serve as an endogenous native ligand for CD33/Siglec 3. Furthermore, forced expansion of MDSC by overexpression of S100A9 in transgenic mice initiates development of hematologic features that phenocopy human MDS, specifically progressive age-dependent ineffective and dysplastic hematopoiesis. These findings indicate that expansion of a single cellular constituent of the BM microenvironment is sufficient to foster neoplastic change in heterologous myeloid progenitors through niche-conductive oncogenesis. The time-dependent accumulation of MDSC in the transgenic mouse model parallels data from recent human studies showing that MDSC expand with age, accompanied by rising serum levels of inflammatory cytokines (e.g., TNF- α , IL-6, and IL-1 β), providing evidence that such senescence-dependent changes driving MDSC expansion may play an important role in the age-dependent predisposition to MDS (35). Importantly, the LIN⁺HLA-DR-CD33⁺ phenotype did not alone confer suppressor cell function, as evidenced by lack of LIN⁺HLA-

DR-CD33⁺ MDSC suppression from age-matched healthy donors or non-MDS cancer patients. Our studies demonstrate the necessity for activation of innate immune signaling and generation of proinflammatory molecules, such as S100A9, for the induction of MDS-MDSC-mediated suppressor function. Furthermore, our finding that primary human MDS-MDSC lack molecular genetic abnormalities intrinsic to the malignant clone indicate that MDSC derive from nonneoplastic HSPC and that MDSC activation and expansion likely precede emergence of genetically distinct MDS clones.

We show, for what we believe is the first time, that CD33, a Siglec receptor expressed by many immune cells including MDSC, is markedly overexpressed by MDS-MDSC and that this receptor controls the suppressive functions of MDS-MDSC through disruption of ITIM-mediated signaling. Additionally, our findings that rhS100A9 directly triggers apoptosis in human HPC indicate that this ligand exerts dual roles in the promotion of ineffective hematopoiesis that involve both cellular (MDSC) and humoral mechanisms (CD33, TLR4). Moreover, cellular response to CD33 ligand engagement appears cell-type specific, i.e., triggering apoptosis in HPC versus activation and proliferation in MDSC. Compensatory regeneration within the myeloid compartment may account for the increased proliferative index observed in MDS (41) and preferential myeloid skewing that occurs with age. Indeed, we found that myeloid mass significantly increased with age in the S100A9Tg mice, accompanied by a significant rise in the proportion of cycling BM precursors (Supplemental Figure 1). We propose a model in which overexpression of CD33 impairs maturation signals from ITAM-associated receptors that is critical to expansion of immature MDSC (Supplemental Figure 3). Consistent with this, shRNA silencing of CD33 reduced myelosuppressive cytokine elaboration and, importantly, restored hematopoietic progenitor colony-forming capacity. Moreover, constitutively active DAP12 signaling was sufficient to override CD33-ITIM inhibition and induce MDSC differentiation, which restored erythropoiesis upon active-DAP12 transfection into MDS-MDSC. DAP12 activation can inhibit TLR-mediated signaling pathways, which may also play a role in inflammation-mediated BM suppression (50, 53).

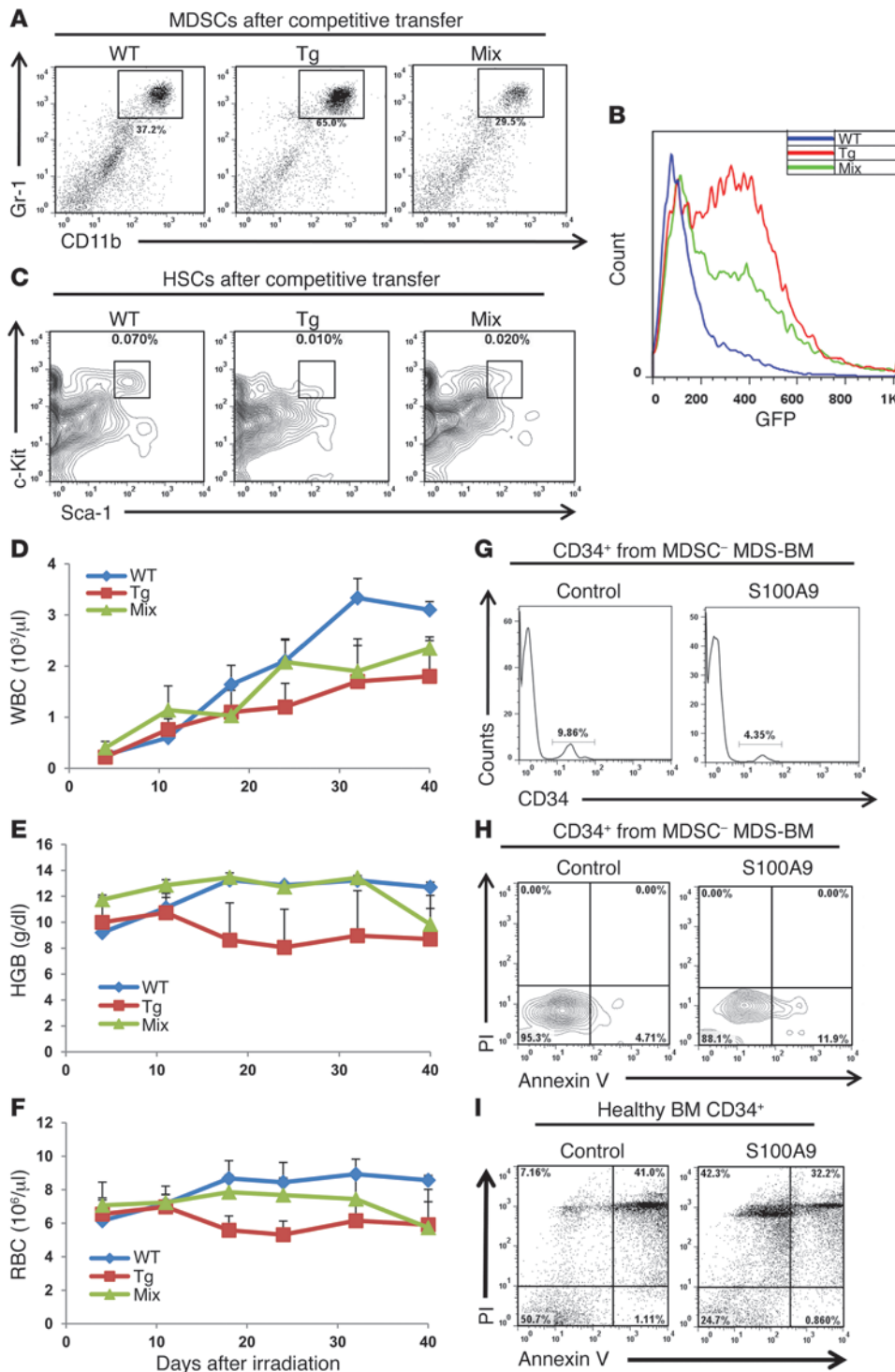


Figure 6

Mix transplant of S100A9- and WT-enriched HSPC continues effects on hematopoiesis. **(A)** Proportion of MDSC in lethally irradiated mice (900 cGy) transplanted with enriched HSPC from WT, S100A9Tg, or a 1:1 mixture of the 2 at 8 weeks (after engraftment). **(B)** GFP expression of MDSC from the experiments in **A**. **(C)** Percentage of KLS stem cells, defined as Lineage⁻cKit⁺Sca-1⁺, in lethally irradiated mice after transplant with WT, S100A9Tg, or 1:1 mix of enriched HSPC. Proportion and concentration of wbc **(D)**, Hgb **(E)**, and rbc **(F)** measured weekly by CBC after transplant. Error bars are the SEM of $n = 5$. **(G)** Percentage of CD34⁺ cells in MDSC-depleted MDS-BM specimens treated with or without S100A9 for 48 hours. **(H)** Same experiment as in **G**, assessing surface expression of annexin V and PI after treatment with S100A9. **(I)** Healthy human CD34 cells were treated as in **H** and cultured for 48 hours followed by annexin V/PI flow cytometric analysis.

Mounting evidence implicates activation of innate immune signaling in the pathogenesis and biologic features of human MDS (7-9). In del(5q) MDS, allelic deletion of miRNA-145 and miRNA-146a results in derepression of the respective targets, TIRAP and TRAF6. Of particular importance, Starczynowski and colleagues showed that knockdown of these specific miRNAs or overexpression of TRAF6 in murine HSPC recapitulated hematologic features of del(5q) MDS in a transplant model through

both cell-autonomous and nonautonomous mechanisms involving IL-6 (10, 54). A recent study showed that IRAK1, a TLR4 adaptor kinase, is overexpressed and hyperactivated in MDS and that IRAK1 inhibition impaired expansion of MDS HPC, while sparing normal CD34⁺ cells (55). Our studies show that the heterodimeric DAMP S100A8/S100A9, specifically released at BM inflammatory sites, is not only aberrantly expressed in MDS but serves as a native ligand for CD33 and a critical effector of



MDSC expansion and HPC apoptosis. This finding provides evidence that S100 proteins contribute directly to MDS pathogenesis through microenvironment-directed, cell-nonautonomous mechanisms involving MDSC (18, 56). Moreover, TLR activation suppresses osteoblast differentiation, while instructing myeloid commitment in HSPC (12, 13). Prolonged activation of innate immune signaling with age, therefore, may disrupt the BM endosteal niche-supporting maintenance of HSPC quiescence and favor translocation of myeloid progenitors to an angiogenic niche characteristic of MDS (57). Our findings of a skewed distribution of cycling precursors along the endosteal region in S100A9Tg mice, coupled with the myeloid lineage expansion with age support this notion. More importantly, the competitive transplant experiments showed that admixture of S100A9Tg with WT donor HSPC delays suppression of hematopoiesis.

Our findings support a model for MDS pathogenesis in which sustained activation of innate immune signaling in the BM microenvironment creates a permissive inflammatory milieu that is sufficient for development of myelodysplasia. Cell-autonomous neoplastic hematopoietic progenitors may emerge following acquisition of secondary genetic abnormalities in the myeloid compartment. S100A9Tg mice simulate human MDS and can serve as an *in vivo* model for studying MDS pathogenesis and development of novel therapeutics. Nevertheless, our data suggest that therapeutic interventions that promote MDSC maturation may have remitting potential when applied early in the disease course.

Methods

MDS patients. The majority of patients with MDS were low risk unless otherwise specified. All patients were confirmed by central review and classified in accordance with either the World Health Organization criteria or the International Prognostic Scoring System (IPSS). Patients were recruited from the Malignant Hematology clinic at the H. Lee Moffitt Cancer Center & Research Institute and the Radboud University Nijmegen Medical Centre, Department of Hematology. BM-MNC were isolated from heparinized BM aspirates by Ficoll-Hypaque gradient centrifugation, as previously described (58). MDSC were defined and purified by FACS of CD33⁺ cells lacking expression of lineage (Lin⁻) markers (CD3, CD14, CD16, CD19, CD20, CD56) and HLA-DR.

Mice. WT FVB/NJ mice were purchased from Jackson Laboratories, and S100A9KO mice and S100A9Tg mice were generated and used as previously described (37, 38). S100A9Tg mice were generated from FVB/NJ homozygous mice and bred for more than 15 generations. Each experiment group included 5 to 10 mice. For the competitive adoptive transplant experiment, 18-week-old FVB/NJ WT female mice were irradiated once in a rotating gamma irradiator for a total dose of 900 cGy. Concurrently, BM cells were isolated from the tibias and femurs of age-matched male WT or S100A9Tg mice from which HSPC were then enriched by magnetic cell sorting (MACS; Miltenyi Biotec) following the manufacturer's protocol. Six hours after irradiation, 1×10^7 enriched HSPC were given by tail vein injection into recipient mice. Mice were then monitored every other day with weight measurements under a sterile hood. Peripheral blood for CBC was collected from the anteroorbital vein by Vivarium staff at the center weekly. By 8 weeks (after which the WT recipients were engrafted, $wbc > 3 \times 10^3$ cells/ml of blood), mice were euthanized by CO₂ aspiration, at which point peripheral blood was collected by heart puncture followed by dissection of tibias and femurs (as before) and spleen for assessment.

FISH. FISH was done at the Cytogenetics Laboratory of Moffitt Cancer Center, and detailed methods have been previously described (58). Target DNA from MDSC-positive (MDS-MDSC) cells and MDSC-negative cells

was purified from the same patients who were previously confirmed to have del5q or del7q using a commercially available test (Abbott Laboratory).

Immunostaining. BM-MNC were purified from MDS patients, diluted to a concentration of 3×10^5 cells/ml, cytospinned onto microscope slides and fixed with methanol/acetone (3:1 ratio at -20°C for 30 minutes). Washes were done with Triton X-100 buffer for 5 minutes and 50 mM Tris buffer (pH 7.4) for 10 minutes prior to blocking for nonspecific binding with serum. We stained the slides with the following primary antibodies: rabbit anti-CD33 antibody (1:100 dilution; Santa Cruz Biotechnology Inc.); mouse anti-granzyme B (1:100 dilution; Fitzgerald Industries); and mouse anti-human CD71 (1:100 dilution; BD Biosciences). This was followed by their respective secondary antibodies: Alexa Fluor 594 goat anti-rabbit IgG (Invitrogen); FITC goat anti-mouse (Sigma-Aldrich); and Alexa Fluor 350 goat anti-mouse IgG (Molecular Probes). Rat anti-human glycophorin A was pre-conjugated to Alexa Fluor 647 using a kit from Molecular Probes before addition to the sample (1:50 dilution; AbD Serotec) followed by mounting the slides with aqueous medium (Molecular Probes). Immunofluorescence was detected using a Zeiss automated upright fluorescence microscope and images captured by a Nikon camera with the capture program AxioVision.

Immunostaining on S100A9 transfected SJCRH30 cells. Detailed methods have been published previously (25). Specifically, SJCRH30 cells that lack detectable expression levels of both CD33 and S100A9 were transfected with either S100A9 or S100A8 (negative control) for 48–72 hours. After incubation with CD33-fusion for 30 minutes (2 µg/ml) they were stained with a secondary anti-human IgG1-APC before analysis by immunofluorescence microscopy. Similarly, SJCRH30 cells, stable-transfected with CD33, were incubated with rhS100A9 tagged with DDK for various time points and stained by the same methodology before analysis.

Suppression assays. To determine whether MDSC are capable of mediating T cell suppression, MDSC were sorted from full BM of MDS patients by FACS. T cells were isolated by MACS using CD3 microbeads (Miltenyi Biotec) from autologous peripheral blood. 2×10^4 T cells were seeded in 96-well round-bottom plates in triplicate in Iscove's modified Dulbecco medium (IMDM; Invitrogen) supplemented with 10% human serum PAA (PAA Laboratories). Cultures were stimulated with 30 U/ml IL-2 (Chiron) and anti-CD3/anti-CD28-coated beads (Invitrogen) at a 1:2 ratio of T cells to beads. MDSC were admixed with T cell cultures at ratios of 1:2 and 1:4. After 3 days of coculture, supernatants were harvested to measure IFN-γ concentration by ELISA (Pierce Endogen). Subsequently, 0.5 µCi ³H-thymidine (PerkinElmer) was added to each well, and after overnight incubation, ³H-thymidine incorporation was measured using a 1205 Wallac Betaplate counter (PerkinElmer). To determine whether differences in proliferation and IFN-γ production were statistically significant, 1-way ANOVA with Bonferroni's post-hoc test was used. $P < 0.05$ was considered significant.

Colony-forming assay. Cells isolated from either human BM or from S100A9Tg, S100A9KO, or WT tibias and femurs were seeded into complete methylcellulose medium (MethoCult complete medium with necessary cytokines and growth factors; StemCell Technologies) following the manufacturer's instructions. After incubation, colonies of BFU-E and GM-CFU were counted using an inverted light microscope.

Real-time quantitative PCR. RNA was isolated by Trizol isolation (Invitrogen) followed by iScript cDNA synthesis (Bio-Rad) and amplification using iQ SYBR Green Supermix (Bio-Rad). The relative level of gene expression for each experimental sample was calculated by the ΔΔCt method, where untreated cells were the experimental control and the housekeeping gene GAPDH was the internal control. Error bars represent the SEM of 3 separate experiments.

Preparation of the CD33/Siglec 3 chimeric fusion protein. Recombinant soluble fusion of CD33/Siglec 3 ectodomain was constructed as described previously (59–61). Specifically, cDNA fragments encoding CD33/Siglec 3

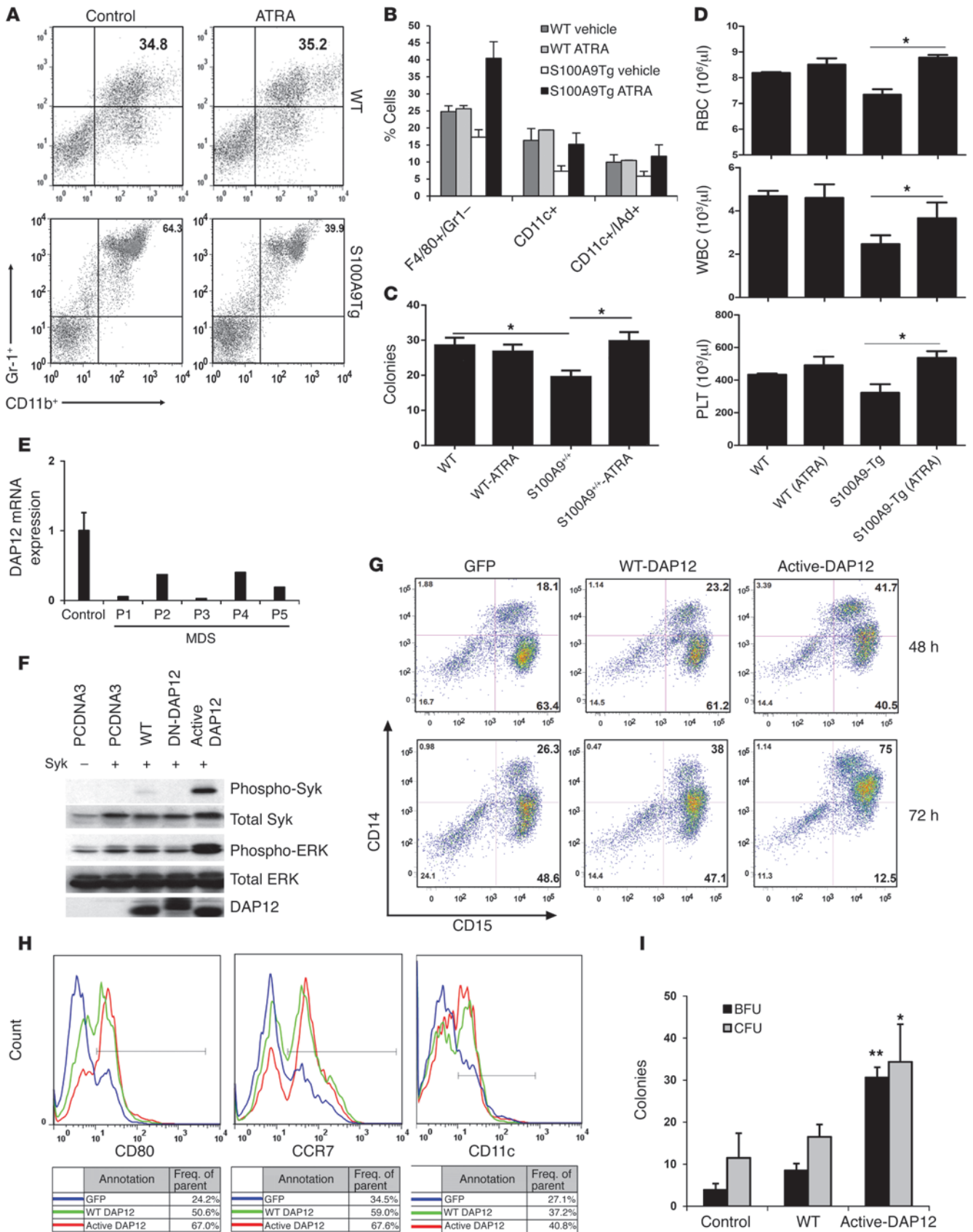




Figure 7

Targeting MDSC activation and signaling can improve suppressive BM microenvironment. ATRA decreases MDSC in the BM of S100A9Tg mice (A) and promotes the expression of myeloid maturation markers (B). (C) BFU colony formation of WT and S100A9Tg mouse BM cells treated with ATRA. All of the cultures were duplicates. * $P < 0.05$, between ATRA-treated and vehicle-treated S100A9Tg mice and (D) the number of rbc, wbc, and platelets from CBC analysis of ATRA-treated and untreated mice. * $P < 0.05$, between ATRA-treated and vehicle-treated S100A9Tg mice. (E) Relative expression levels of DAP12 from isolated MDSC from either healthy or MDS specimens by qPCR ($n = 5$). (F) AD293 cells were transfected with either vector, WT-DAP12, dominant negative (DN) DAP12, or active DAP12 (P23) for 48 hours and analyzed by Western blot for the expression of phosphorylated or total Syk and ERK. This is representative of 3 independent experiments. MDSC were isolated from the BM of MDS patients and infected with adenoviral vector containing either WT or active DAP12 (P23) for 48 or 72 hours. The surface expression of CD14 or CD15 (G) or the maturation markers CD80, CCR7, and CD11c (H) was then analyzed by flow cytometry. (I) MDSC were purified from BM-MNC of MDS patients by FACS sorting, and cells were infected with LV-WT DAP12 or LV-P23. Colony formation assays were performed in methylcellulose for 14 days. Results are shown as mean \pm SEM of 7 patients. * $P < 0.01$; ** $P < 0.001$, versus cells infected with LV-WT.

ectodomain were amplified by PCR and inserted into a vector that encodes the human Fc γ followed by a C terminal recognition site for *E. coli* biotin ligase. This vector has been engineered to facilitate the fusion of gene segments encoding extracellular Ig-type domains to the Fc region of human IgG1. The recombinant proteins were expressed in 293T cells after transfection, using Lipofectamine (Invitrogen), with 3 successive harvests of 25 ml OPTI-MEM I serum-free medium. The harvests were pooled, centrifuged at 500 g for 10 minutes to remove debris, and stored at 4°C in 0.02% sodium azide. Concentrations of CD33-fusions in culture supernatants were determined by Bradford assay (Bio-Rad).

Mass spectrometry. Following in-gel tryptic digestion, peptides were extracted and concentrated under vacuum centrifugation. A nanoflow liquid chromatograph (Easy-nLC; Proxeon) coupled to an electrospray ion trap mass spectrometer (LTQ; Thermo) was used for tandem mass spectrometry peptide sequencing experiments. The sample was first loaded onto a trap column (BioSphere C18 reversed phase resin, 5 μ m, 120 Å, 100 μ m ID; NanoSeparations) and washed for 3 minutes at 8 ml/min. The trapped peptides were eluted onto the analytical column (BioSphere C18 reversed-phase resin, 150 mm, 5 μ m, 120 Å, 100 μ m ID; NanoSeparations). Peptides were eluted in a 60-minute gradient from 5% B to 45% B (solvent A: 2% acetonitrile + 0.1% formic acid; solvent B: 90% acetonitrile + 0.1% formic acid) with a flow rate of 300 nl/min. Five tandem mass spectra were collected in a data-dependent manner following each survey scan. Sequences were assigned using Mascot (www.matrixscience.com) searches against human IPI entries. Carbamidomethylation of cysteine, methionine oxidation, and deamidation of asparagine and glutamine were selected as variable modifications, and as many as 2 missed tryptic cleavages were allowed. Precursor mass tolerance was set to 2.5 and fragment ion tolerance to 0.8. Results from Mascot were compiled in Scaffold, which was used for manual inspection of peptide assignments and protein identification.

Identification of specific binding of S100A9 to CD33/Siglec 3. Ninety-six-well flat-bottom ELISA plates were coated overnight with 1 μ g/ml of monoclonal anti-S100A9, as per the manufacturer's suggestions. After washing with 1 \times PBS-T, 50 μ l of lysates from untransfected cells (negative) or S100A9 transfected cells was added to the wells. Secondary antibody was either a S100A9 polyclonal antibody (positive control) or CD33-fusion as indicated followed by ELISA HRP reaction analysis at 440 nm.

Preparation of adenoviral vector expressing CD33. CD33 plasmid (GeneCopeia) was subcloned into a pShuttle-IRES-hrGFP-1 vector (containing the CMV promoter and hrGFP). The PmeI-digested shuttle vectors were then cotransformed into electrocompetent BJ5183 bacteria with pAdEasy-1 (containing the viral backbone) and selected on Kanamycin LB plates. The plasmid in the bacteria was amplified and purified using a plasmid maxiprep system (QIAGEN). The complete adenoviral vector was linearized by PacI digestion and then transfected into AD293 cells using Lipofectamine (Invitrogen). All recombinant adenoviruses were amplified in AD293 cells. Viral stocks were obtained by amplification of the AD293 cells followed by standard 2-step CsCl gradient ultracentrifugation, dialysis, and storage in a glycerol stock (10% vol/vol) at -80°C . The titer of each viral stock was routinely tested to be 10^{11} – 10^{12} PFU by plaque-forming assay using AD293 cells.

Preparation of shRNA LVs. SureSilencing shRNA Plasmid for Human S100A8, S100A9, and CD33 and negative control (nontarget) were purchased from SABiosciences. 293T cells were transfected using Attactene reagent (SABiosciences) according to the manufacturer's instructions. Virus containing medium was collected 24–48 hours later. Plasmids, pcDNA3 WT DAP12 and P23-DAP12 were cut with HindIII and XhoI (Promega), and DNA Polymerase I Large (KlenowI) (New England Biolabs Inc.) was used to fill in recessed 3' ends of DNA fragments. pWPI, which contains a GFP expression cassette (Addgene Organization), was digested using PmeI (New England Biolabs Inc.). After cutting DNA and DNA, pWPI was purified by Strata Prep PCR purification kit (QIAGEN), DNAs were ligated (Takara DNA Ligation Kit; Fisher) into vector pWPI, and STBL2 competent cells were transformed (Invitrogen). 293T cells were transfected with pWPI lentivirus vector, the packaging plasmid psPAX2, and the envelope plasmid pMD2.G (Addgene Organization) using Lipofectamine 2000 (Invitrogen) at a ratio of 4:3:1 according to standard protocols. Four days after the first infection, transduced cells were isolated by FACS sorting GFP⁺ cells with greater than 99% purity.

Infection of MDSC from MDS patients. MDSC isolated from MDS patients were infected 3 times using virus-containing infection medium at 24-hour intervals in the presence of 8 μ g/ml polybrene. For each infection, cells were plated in 12-well dishes at 1×10^6 cells/well. Four days after the first infection, cells were harvested and used for qPCR, Western blot analysis, flow cytometry, or colony formation assays.

Flow cytometry. BM-MNC were stained with appropriate specific conjugated antibodies in PBS with 2% BSA buffer. For MDSC sorting, FITC anti-CD33 and FITC anti-HLA-DR were used as positive controls and isotype IgG was used for negative control and to detect nonspecific staining. Sorting was performed on a FACSAria cell sorter by Core facility personnel. For antigenic determination, cells were washed in PBS and then stained with PE-conjugated mAbs specific to CD40, CD80, CD83, CD86, CCR7, CD11c, CD14, HLA-DR, TLR2, or TLR4 and relevant isotype controls (eBioscience) for 30 minutes in the dark, on ice. Live cells were gated based on negative staining for 7-AAD. Samples were acquired on a FACSCalibur flow cytometer, and the analysis was performed using FlowJo 6.3.4 software.

Arginase activity. Arginase activity was measured in cell lysates as previously described (62). In brief, cells were lysed for 30 minutes with 100 μ l of 0.1% Triton X-100. Subsequently, 100 μ l of 25 mM Tris-HCl and 10 μ l of 10 mM MnCl₂ were added, and the enzyme was activated by heating for 10 minutes at 56°C. Arginine hydrolysis was conducted by incubating the lysate with 100 μ l of 0.5 M L-arginine (pH 9.7) at 37°C for 120 minutes. The reaction was stopped with 900 μ l of H₂SO₄ (96%)/H₃PO₄ (85%)/H₂O (1/3/7, v/v/v). Urea concentration was measured at 540 nm after addition of 40 μ l of α -isonitrosopropiophenone, followed by heating at 95°C for 30 minutes.

NO production. Equal volumes of culture supernatants (100 μ l) were mixed with Greiss reagent solution (1% sulfanilamide in 5% phosphoric acid and 0.1% N-1-naphthylethylenediamine dihydrochloride) in double-



distilled water and incubated for 10 minutes at room temperature. Absorbance of the mixture was measured at 550 nm using a microplate reader (Bio-Rad). Nitrite concentrations were determined by comparing the absorbance values for the test samples to a standard curve generated by serial dilution of 0.25 mM sodium nitrite.

Western blot analysis. Cell lysates were prepared by resuspending cell pellets in 1% NP-40, 10 mM Tris, 140 mM NaCl, 0.1 mM PMSF, 10 mM iodoacetamide, 50 mM NaF, 1 mM EDTA, 0.4 mM sodium orthovanadate, 10 µg/ml leupeptin, 10 µg/ml pepstatin, and 10 µg/ml aprotinin and lysing on ice for 30 minutes. Cell lysates were centrifuged at 12,000 g for 15 minutes to remove nuclei and cell debris. The protein concentration of the soluble extracts was determined by using the Bio-Rad (Bradford) protein assay. 50 µg of protein (per lane) was separated on a 10% SDS-polyacrylamide gel by electrophoresis, then transferred to a PVDF membrane. Membranes were probed for indicated antibody: anti-S100A8, anti-S100A9, or anti-S100A8/A9 (Santa Cruz Biotechnology Inc.); anti-phospho ERK, anti-total ERK, anti-phospho Syk, and anti-total Syk (Cell Signaling). Proteins were detected with the enhanced chemiluminescence detection system (ECL; Amersham).

In vitro dot blotting analysis of direct binding of S100A9 to CD33. Lysate from S100A9 untransfected, empty vector, and S100A9 transfect SJC1RH30 or AD293 cells was serially diluted (as indicated in Figure 3) with the first lysate, starting at 50 µg, followed by loading onto a nitrocellulose membrane and blocking overnight at 4°C in 5% milk. Following incubation with CD33-fusion for 2 hours at room temperature, and staining with an anti-human IgG HRP-conjugated secondary, the membrane was washed and used for radiograph analysis to demonstrate specific S100A9 binding to CD33. The membrane was afterwards used for Coomassie blue staining to show the relative equal loading of proteins on each dot in the nitrocellulose membrane.

CBC. CBC was performed by animal core laboratory pathological personnel in the Vivarium at the Moffitt Cancer Center. The mouse blood parameters were determined as described in Supplemental Table 1 with a Heska Hematrue Hematology Analyzer.

Pathological examination of spleen and BM biopsy from WT and S100A9Tg mice. BM cells were obtained from bilateral tibiae and femura from 6-month-old S100A9Tg and WT control mice as previously described (63). Touch prints of murine splenocytes were prepared as described elsewhere (64). BM aspirates and touch imprints were stained using Wright-Giemsa stain. Sections of BM and spleen were fixed in 10% phosphate-buffered neutral formalin, decalcified (only applied to BM), and embedded in paraffin by routine procedures. Sections were cut at 4 µm and stained with H&E and PAS. The presence of myelodysplastic features characteristic of MDS was evaluated by an experienced hematopathologist. Comparisons of the hematopathological analysis of WT (Figure 5, G–J) and S100A9Tg (Figure 5, K–N) were performed at Moffitt's hematopathology clinical research laboratories. BM core biopsy showed 50% cellularity with maturing trilineage hematopoiesis (H&E, ×200). Figure 5H shows a high-power view of the BM biopsy that demonstrates normal-appearing megakaryocytes with normal lobation.

Mixed myeloid and erythroid precursors are normally distributed with estimated M/E ratio of 2:1 (H&E, ×600). Wright-Giemsa-stained BM aspirate exhibited full maturation in all 3 lineages without dysplastic features (Wright-Giemsa, ×1000; Figure 5I). Inlet showed a normal lobated megakaryocyte. Touch imprint of mouse spleen displayed predominance of small and mature-appearing lymphocytes intermingled with occasional erythropoietic precursors (Wright-Giemsa, ×1000; Figure 5J). S100A9Tg mice BM core biopsy revealed hypercellularity, approximately 95% with increased megakaryocytes, especially in small forms (H&E, ×200; Figure 5K). High-power magnification highlighted dysplastic megakaryocytes with single, hypolobated, or disjointed nuclei and markedly increased in number (H&E, ×600, insert; Figure 5L). Inlet included 2 markedly dysplastic micro-megakaryocytes with hypolobation. BM aspirates exhibited mildly increased blasts admixed with myeloid and erythroid precursors (Figure 5M). The latter demonstrated slightly irregular nuclear contour and minimal megaloblastoid changes (Wright-Giemsa, ×1000). Inlet (insert) contained 2 blasts showing delicate or fine chromatin, prominent nucleoli, a high N/C ratio, and scant basophilic cytoplasm. Touch preparation of transgenic mouse spleen showed increased erythroid precursors; some of them displaying enlarged size with abnormal nuclearity and occasional nuclear bridge (Wright-Giemsa, ×1000; Figure 5N).

Statistics. All data are presented as mean ± SEM. Statistical calculations were performed with Microsoft Excel or GraphPad Prism analysis tools. Differences between individual groups were analyzed by paired *t* test. *P* < 0.05 was considered statistically significant.

Study approval. All mouse experiments were approved by the Institutional Animal Care and Use Committee at the University of South Florida.

Acknowledgments

This work was supported by NIH grants R01CA131076, R01CA100062, and AI056213. Erika Eksioglu and Sarah Donatelli (née Rasche) were supported through the T32 training grant CA115308. The Moffitt Proteomics Facility is supported by the US Army Medical Research and Materiel Command under award no. DAMD17-02-2-0051 for a National Functional Genomics Center, the National Cancer Institute under award no. P30-CA076292 as a Cancer Center Support Grant, and the Moffitt Foundation. The triple quadrupole mass spectrometer was purchased with a shared instrument grant from the Bankhead-Coley Cancer Research program of the Florida Department of Health (06BS-02-9614).

Received for publication October 29, 2012, and accepted in revised form August 15, 2013.

Address correspondence to: Sheng Wei, H. Lee Moffitt Cancer Center, MRC 4072, 12902 Magnolia Dr., Tampa, Florida 33647, USA. Phone: 813.745.3934; Fax: 813.745.7264; E-mail: sheng.wei@moffitt.org.

- Allampallam K, et al. Biological significance of proliferation, apoptosis, cytokines, and monocyte/macrophage cells in bone marrow biopsies of 145 patients with myelodysplastic syndrome. *Int J Hematol.* 2002;75(3):289–297.
- Navas T, et al. Inhibition of p38alpha MAPK disrupts the pathological loop of proinflammatory factor production in the myelodysplastic syndrome bone marrow microenvironment. *Leuk Lymphoma.* 2008;49(10):1963–1975.
- Stirewalt DL, et al. Tumour necrosis factor-induced gene expression in human marrow stroma: clues to the pathophysiology of MDS? *Br J Haematol.* 2008; 140(4):444–453.
- Kristinsson SY, Björkholm M, Hultcrantz M, Derolf ÅR, Landgren O, Goldin LR. Chronic immune stimulation might act as a trigger for the development of acute myeloid leukemia or myelodysplastic syndromes. *J Clin Oncol.* 2011;29(21):2897–2903.
- Takizawa H, Boettcher S, Manz MG. Demand-adapted regulation of early hematopoiesis in infection and inflammation. *Blood.* 2012;119(13):2991–3002.
- Maratheftis CI, Andreacos E, Moutsopoulos HM, Voulgarelis M. Toll-like receptor-4 is up-regulated in hematopoietic progenitor cells and contributes to increased apoptosis in myelodysplastic syndromes. *Clin Cancer Res.* 2007;13(4):1154–1160.
- Hofmann WK, de Vos S, Komor M, Hoelzer D, Wachsman W, Koeffler HP. Characterization of gene expression of CD34+ cells from normal and myelodysplastic bone marrow. *Blood.* 2002; 100(10):3553–3560.
- Gondek LP, Tiu R, O'Keefe CL, Sekeres MA, Theil KS, Maciejewski JP. Chromosomal lesions and uniparental disomy detected by SNP arrays in MDS, MDS/MPD, and MDS-derived AML. *Blood.* 2008; 111(3):1534–1542.
- Starczynowski DT, et al. High-resolution whole genome tiling path array CGH analysis of CD34+ cells from patients with low-risk myelodysplastic syndromes reveals cryptic copy number alterations and predicts overall and leukemia-free survival.



- Blood*. 2008;112(8):3412–3424.
10. Starczynowski DT, et al. Identification of miR-145 and miR-146a as mediators of the 5q-syndrome phenotype. *Nat Med*. 2010;16(1):49–58.
 11. Fang J, et al. Cytotoxic effects of bortezomib in myelodysplastic syndrome/acute myeloid leukemia depend on autophagy-mediated lysosomal degradation of TRAF6 and repression of PSMA1. *Blood*. 2012;120(4):858–867.
 12. Bandow K, et al. Molecular mechanisms of the inhibitory effect of lipopolysaccharide (LPS) on osteoblast differentiation. *Biochem Biophys Res Commun*. 2010;402(4):755–761.
 13. De Luca K, et al. The TLR1/2 agonist PAM(3)CSK(4) instructs commitment of human hematopoietic stem cells to a myeloid cell fate. *Leukemia*. 2009;23(11):2063–2074.
 14. Dykstra B, Olthof S, Schreuder J, Ritsema M, de Haan G. Clonal analysis reveals multiple functional defects of aged murine hematopoietic stem cells. *J Exp Med*. 2011;208(13):2691–2703.
 15. Gabrilovich DI, Nagaraj S. Myeloid-derived suppressor cells as regulators of the immune system. *Nat Rev Immunol*. 2009;9(3):162–174.
 16. Kusmartsev S, Gabrilovich DI. Role of immature myeloid cells in mechanisms of immune evasion in cancer. *Cancer Immunol Immunother*. 2006;55(3):237–245.
 17. Vogl T, et al. Mrp8 and Mrp14 are endogenous activators of Toll-like receptor 4, promoting lethal, endotoxin-induced shock. *Nat Med*. 2007;13(9):1042–1049.
 18. Ehrchen JM, Sunderkotter C, Foell D, Vogl T, Roth J. The endogenous Toll-like receptor 4 agonist S100A8/S100A9 (calprotectin) as innate amplifier of infection, autoimmunity, and cancer. *J Leukoc Biol*. 2009;86(3):557–566.
 19. Kapanadze T, et al. Regulation of accumulation and function of myeloid derived suppressor cells in different murine models of hepatocellular carcinoma. *J Hepatol*. 2013;pii:S0168-8278(13)00421-2.
 20. Sade-Feldman M, Kanterman J, Ish-Shalom E, Elnekave M, Horwitz E, Baniyash M. Tumor necrosis factor- α blocks differentiation and enhances suppressive activity of immature myeloid cells during chronic inflammation. *Immunity*. 2013;38(3):541–554.
 21. Talmadge JE. Pathways mediating the expansion and immunosuppressive activity of myeloid-derived suppressor cells and their relevance to cancer therapy. *Clin Cancer Res*. 2007;13(18 pt 1):5243–5248.
 22. Talmadge JE, Donkor M, Scholar E. Inflammatory cell infiltration of tumors: Jekyll or Hyde. *Cancer Metastasis Rev*. 2007;26(3–4):373–400.
 23. Crocker PR, Paulson JC, Varki A. Siglecs and their roles in the immune system. *Nat Rev Immunol*. 2007;7(4):255–266.
 24. Ostrand-Rosenberg S, Sinha P. Myeloid-derived suppressor cells: linking inflammation and cancer. *J Immunol*. 2009;182(8):4499–4506.
 25. Chen X, et al. A critical role for DAP10 and DAP12 in CD8⁺ T cell-mediated tissue damage in large granular lymphocyte leukemia. *Blood*. 2009;113(14):3226–3234.
 26. Blasius AL, Cella M, Maldonado J, Takai T, Colonna M. Siglec-H is an IPC-specific receptor that modulates type I IFN secretion through DAP12. *Blood*. 2006;107(6):2474–2476.
 27. Blasius AL, Colonna M. Sampling and signaling in plasmacytoid dendritic cells: the potential roles of Siglec-H. *Trends Immunol*. 2006;27(6):255–260.
 28. Lajaunias F, Dayer JM, Chizzolini C. Constitutive repressor activity of CD33 on human monocytes requires sialic acid recognition and phosphoinositide 3-kinase-mediated intracellular signaling. *Eur J Immunol*. 2005;35(1):243–251.
 29. Nutku E, Aizawa H, Hudson SA, Bochner BS. Ligation of Siglec-8: a selective mechanism for induction of human eosinophil apoptosis. *Blood*. 2003;101(12):5014–5020.
 30. von Gunten S, Bochner BS. Basic and clinical immunology of Siglecs. *Ann N Y Acad Sci*. 2008;1143:61–82.
 31. Paul SP, Taylor LS, Stansbury EK, McVicar DW. Myeloid specific human CD33 is an inhibitory receptor with differential ITIM function in recruiting the phosphatases SHP-1 and SHP-2. *Blood*. 2000;96(2):483–490.
 32. Ulyanova T, Shah DD, Thomas ML. Molecular cloning of MIS, a myeloid inhibitory siglec, that binds protein-tyrosine phosphatases SHP-1 and SHP-2. *J Biol Chem*. 2001;276(17):14451–14458.
 33. Avril T, Floyd H, Lopez F, Vivier E, Crocker PR. The membrane-proximal immunoreceptor tyrosine-based inhibitory motif is critical for the inhibitory signaling mediated by Siglecs-7 and -9. CD33-related Siglecs expressed on human monocytes and NK cells. *J Immunol*. 2004;173(11):6841–6849.
 34. Ikehara Y, Ikehara SK, Paulson JC. Negative regulation of T cell receptor signaling by Siglec-7 (p70/AIRM) and Siglec-9. *J Biol Chem*. 2004;279(41):43117–43125.
 35. Verschoor CP, et al. Blood CD33(+)HLA-DR(-) myeloid-derived suppressor cells are increased with age and a history of cancer. *J Leukoc Biol*. 2013;93(4):633–637.
 36. Lagasse E, Clerc RG. Cloning and expression of two human genes encoding calcium-binding proteins that are regulated during myeloid differentiation. *Mol Cell Biol*. 1988;8(6):2402–2410.
 37. Cheng P, et al. Inhibition of dendritic cell differentiation and accumulation of myeloid-derived suppressor cells in cancer is regulated by S100A9 protein. *J Exp Med*. 2008;205(10):2235–2249.
 38. Manitz MP, et al. Loss of S100A9 (MRP14) results in reduced interleukin-8-induced CD11b surface expression, a polarized microfilament system, and diminished responsiveness to chemoattractants in vitro. *Mol Cell Biol*. 2003;23(3):1034–1043.
 39. Byrne P, et al. Chimerism analysis in sex-mismatched murine transplantation using quantitative real-time PCR. *BioTechniques*. 2002;32(2):279–280.
 40. Lambert JF, Benoit BO, Colvin GA, Carlson J, Delville Y, Quesenberry PJ. Quick sex determination of mouse fetuses. *J Neurosci Methods*. 2000;95(2):127–132.
 41. Raza A, et al. Apoptosis in bone marrow biopsy samples involving stromal and hematopoietic cells in 50 patients with myelodysplastic syndromes. *Blood*. 1995;86(1):268–276.
 42. Raza A, et al. Novel insights into the biology of myelodysplastic syndromes: excessive apoptosis and the role of cytokines. *Int J Hematol*. 1996;63(4):265–278.
 43. Shetty V, et al. Intramedullary apoptosis of hematopoietic cells in myelodysplastic syndrome patients can be massive: apoptotic cells recovered from high-density fraction of bone marrow aspirates. *Blood*. 2000;96(4):1388–1392.
 44. Nefedova Y, Fishman M, Sherman S, Wang X, Beg AA, Gabrilovich DI. Mechanism of all-trans retinoic acid effect on tumor-associated myeloid-derived suppressor cells. *Cancer Res*. 2007;67(22):11021–11028.
 45. Mirza N, et al. All-trans-retinoic acid improves differentiation of myeloid cells and immune response in cancer patients. *Cancer Res*. 2006;66(18):9299–9307.
 46. Lanier LL. NK cell recognition. *Annu Rev Immunol*. 2005;23:225–274.
 47. Ravetch JV, Lanier LL. Immune inhibitory receptors. *Science*. 2000;290(5489):84–89.
 48. Angata T, Hayakawa T, Yamanaka M, Varki A, Nakamura M. Discovery of Siglec-14, a novel sialic acid receptor undergoing concerted evolution with Siglec-5 in primates. *FASEB J*. 2006;20(12):1964–1973.
 49. Lanier LL, Corliss BC, Wu J, Leong C, Phillips JH. Immunoreceptor DAP12 bearing a tyrosine-based activation motif is involved in activating NK cells. *Nature*. 1998;391(6668):703–707.
 50. Turnbull IR, Colonna M. Activating and inhibitory functions of DAP12. *Nat Rev Immunol*. 2007;7(2):155–161.
 51. Araki H, et al. Reprogramming of human postmitotic neutrophils into macrophages by growth factors. *Blood*. 2004;103(8):2973–2980.
 52. Raaijmakers MH, et al. Bone progenitor dysfunction induces myelodysplasia and secondary leukemias. *Nature*. 2010;464(7290):852–857.
 53. Hamerman JA, Jarjoura JR, Humphrey MB, Nakamura MC, Seaman WE, Lanier LL. Cutting edge: inhibition of TLR and FcR responses in macrophages by triggering receptor expressed on myeloid cells (TREM)-2 and DAP12. *J Immunol*. 2006;177(4):2051–2055.
 54. Starczynowski DT, Karsan A. Innate immune signaling in the myelodysplastic syndromes. *Hematol Oncol Clin North Am*. 2010;24(2):343–359.
 55. Bolanos L, et al. Targeting IRAK1 as a therapeutic approach for Myelodysplastic Syndrome. *Cancer Cell*. 2013;24(1):90–104.
 56. Viemann D, et al. MRP8/MRP14 impairs endothelial integrity and induces a caspase-dependent and -independent cell death program. *Blood*. 2007;109(6):2453–2460.
 57. Bellamy WT, et al. Vascular endothelial cell growth factor is an autocrine promoter of abnormal localized immature myeloid precursors and leukemia progenitor formation in myelodysplastic syndromes. *Blood*. 2001;97(5):1427–1434.
 58. Wei S, et al. A critical role for phosphatase haploinsufficiency in the selective suppression of deletion 5q MDS by lenalidomide. *Proc Natl Acad Sci USA*. 2009;106(31):12974–12979.
 59. Cannon JP, O'Driscoll M, Litman GW. Specific lipid recognition is a general feature of CD300 and TREM molecules. *Immunogenetics*. 2012;64(1):39–47.
 60. Cannon JP, O'Driscoll M, Litman GW. Construction, expression, and purification of chimeric protein reagents based on immunoglobulin fc regions. *Methods Mol Biol*. 2011;748:51–67.
 61. Cannon JP, et al. A bony fish immunological receptor of the NITR multigene family mediates allogeneic recognition. *Immunity*. 2008;29(2):228–237.
 62. Youn JI, Nagaraj S, Collazo M, Gabrilovich DI. Subsets of myeloid-derived suppressor cells in tumor-bearing mice. *J Immunol*. 2008;181(8):5791–5802.
 63. Xu S, De Becker A, Van Camp B, Vanderkerken K, Van Riet I. An improved harvest and in vitro expansion protocol for murine bone marrow-derived mesenchymal stem cells. *J Biomed Biotechnol*. 2010;2010:105940.
 64. Ioachim HL, Medeiros LJ. Cytopathology. In: *Ioachim's Lymph Node Pathology*. 4th ed. Philadelphia, Pennsylvania, USA: Wolters Kluwer/Lippincott Williams & Wilkins; 2008:21–22.